Deep source regions for back-arc volcanism in the Patagonian slab window imaged by finite frequency P and SH body wave tomography

Walid Ben-Mansour[(1)], Valerie Maupin [(2)], Douglas A Wiens [(1)], Andreas Richter[(3)]

(1) Washington University in Saint Louis, Department of Earth, Environmental and Planetary Sciences, MO, USA.
(2) University of Oslo, PHAB –Centre for Planetary Habitability, Oslo, Norway.
(3) Laboratorio, MAGGIA, Universidad Nacional de La Plata, CONICET, La Plata, Argentina.

Corresponding author: walid@wustl.edu

Deep source regions for back-arc volcanism in the Patagonian slab window imaged by finite frequency P and SH body wave tomography

Walid Ben-Mansour[(1)], Valerie Maupin[(2)], Douglas A Wiens[(1)], Andreas Richter[(3)]

(1) Department of Earth, Environmental and Planetary Sciences, Washington University in Saint Louis, Saint Louis, MO, USA, (2) University of Oslo, PHAB, Oslo, Norway, (3) Laboratorio MAGGIA, Universidad Nacional de La Plata, CONICET, La Plata, Argentina

Abstract

The subduction of the Chile Ridge beneath South America beginning 12-16 Myr ago opened a gap in the subducting slab beneath southern Patagonia, which migrated northward and is located today at 46^{o}S. Geodynamic processes associated with the slab window are poorly understood. Here we apply finite-frequency P and SH body wave tomography to seismic data from several temporary arrays as well as regional stations to image seismic heterogeneities down to 650 km depth. The results show strong low velocity anomalies extending to 400 km depth beneath recent back-arc volcanism between 46^{o}S and 48^{o}S, suggesting a link to thermal upwelling in the upper mantle. The southern edge of the Nazca slab extends aseismically down to at least 350 km. We also image low upper mantle seismic velocities beneath the Patagonia icefields, suggesting low viscosity modulates the patterns of uplift and horizontal deformation observed by GNSS.

Plain summary

The presence of a tear in the downgoing plate brings hot material from the asthenosphere and modifies locally the mantle flow associated with the subduction zone. Patagonia is a good example where the subduction of the spreading ridge created an opening in the slab. Using arrival times of P and S waves, we develop a new seismic model of the mantle in this region. We show strong back-arc low velocity anomalies extending to 400 km depth beneath recent back-arc volcanism between 46^{o}S and 48^{o}S, suggesting this volcanism is linked to upwelling in the upper mantle. We show that the southern edge of the Nazca slab extends to at least 350 km. Additionally, our new model suggests lateral variations in mantle viscosity that help to explain the present-day bedrock deformation across the Patagonia icefield.

1. Introduction

The subduction of a spreading ridge opens a window in the subducting slab, allowing the asthenosphere to upwell and interact with the shallow mantle and crust. Slab windows have a profound influence on geodynamics processes, mantle flow pattern, and thermal structure of subduction zones [Groome and Thorkelson, 2009; Sanhueza et al., 2023]. Magmatism in a slab window is often characterized by adakitic melts associated with slab edges and a volcanic gap in the center of the window [Thorkelson and Breitsprecher, 2005]. Magmatism may shift to the back-arc region, with tholeiitic lavas presumably due to mantle upwelling observed [Gorring et al., 1997; Thorkelson and Breitsprecher, 2005]. However, it is unclear whether this magmatism results from uppermost mantle processes or is instead due to deeper mantle upwelling.

The Patagonia slab window (**Figure 1a**) formed 14 Ma in Southern Patagonia due to the subduction of the Chile Ridge spreading ridge beneath South America and has migrated northward to its present location at 46°-47°S [Breitsprecher and Thorkelson, 2009]. Geochemical studies identified the variation of geochemical signature of magma along the subduction with a transition from adakitic to basaltic signature in the slab melt and presence of an asthenospheric window [Thorkelson and Breitsprecher, 2005]. The back-arc region shows widespread recent volcanic activity with the development of massive plateau lavas [Ramos and Kay 1992; Gorring et al. 1997; Guivel et al., 2006, Guest et al., 2024]. The source of this magmatism and its distinctive geochemical signatures, as well as its relationship to the slab window are not well understood [Gorring et al, 2003; Guest et al. 2024]. From analogue modelling and the compilation of available ages of back-arc magmatism and kinematic reconstruction of the edge of the Antarctic slab, Guillaume et al. (2010) suggest that recent volcanism could be due to lateral flow of sub-slab mantle.

The Patagonian slab window underlies the Northern and Southern Patagonian Icefields (NPI and SPI), so the thermal and rheological perturbations resulting from the window may be important for the solid earth response to the ice load [Klemann et al., 2007; Lange et al, 2014; Mark et al., 2022; Russo et al, 2022]. Currently the NPI and SPI are undergoing rapid ice mass loss [Richter et al. 2019], associated with a fast bedrock uplift [Dietrich et al. 2010; Richter et al. 2016]. The intensity of the solid-earth response to the glacial retreat can be explained by the regional scale rheology with low viscosity in the asthenosphere and a thin lithosphere [Lange et al. 2014; Mark et al., 2022; Russo et al., 2022].

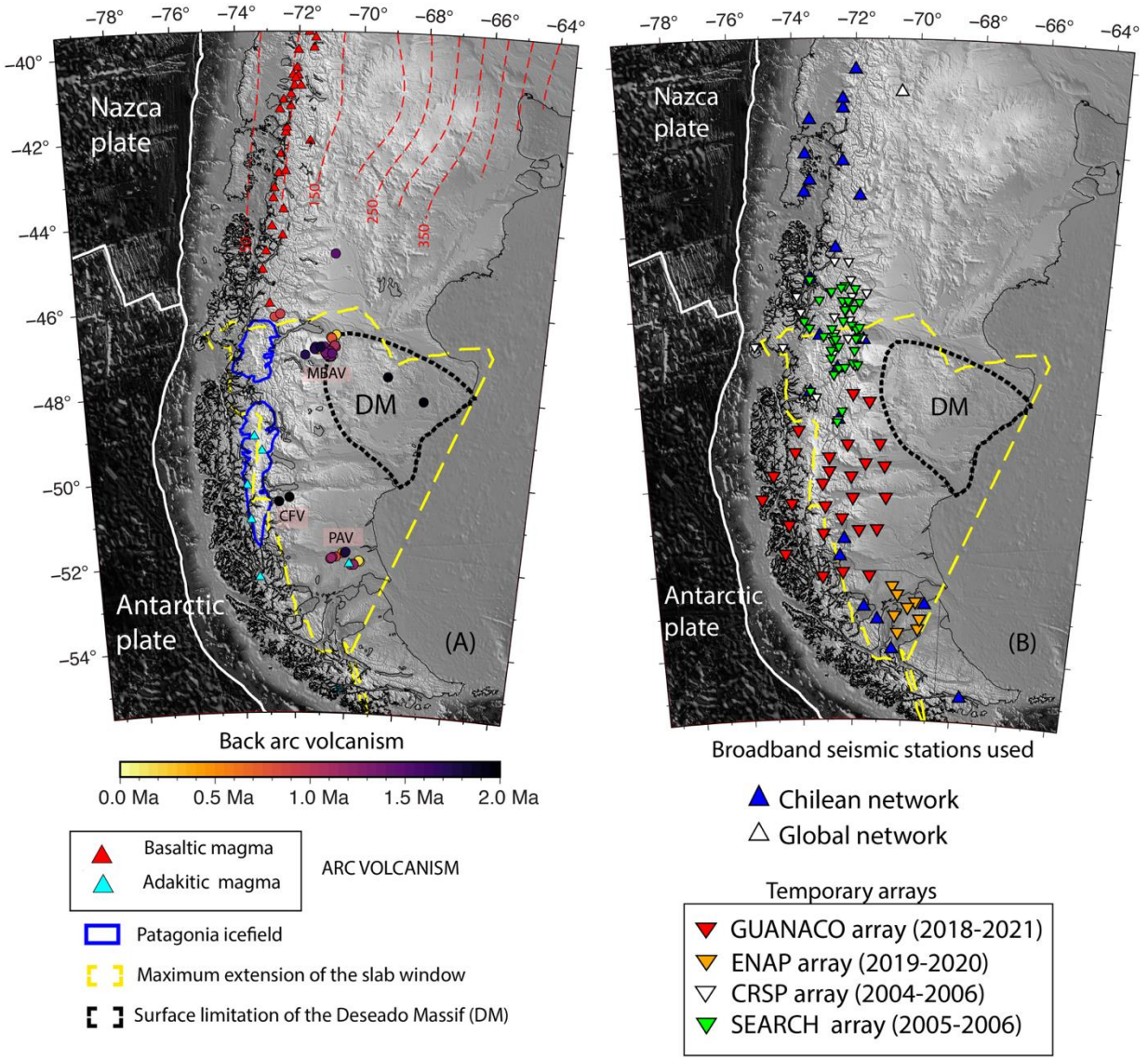

Figure 1. *(Left) Topographic map of Southern Patagonia with main tectonics features.* Red dashed lines represent iso-depth of the Nazca slab (50 km interval) from Portner et al. (2020). Yellow dashed lines represent the maximum extension of the slab window from Breitsprecher *and Thorkelson (2009). Colored circles represent young back-arc volcanism (<2Myrs) from Guillaume et al. (2010). MBAV: Meseta del Lago Buenos Aires Volcanic field, CFV: Cerro del Fraile volcanics, PAV: Pali Aike Volcanic field. (Right) Broadband seismic stations used in this study.*

A recent regional scale Rayleigh wave imaging study [Mark et al., 2022] shows the presence of a low velocity anomaly in the uppermost mantle which is interpreted as a thermal erosion of the lithospheric mantle over the youngest part of the slab window. From shear wave splitting

analysis, Ben-Mansour et al. (2022) found strong anisotropy with low uppermost mantle shear velocities and an absence of mantle lithosphere. In addition, other studies have imaged the structure immediately beneath the Chile Triple Junction (CTJ) [Russo et al., 2010; Miller et al., 2023]. In the recent years, new continent-scale models have been proposed using finite frequency tomography [Portner et al. 2020; Rodriguez et al., 2021; Kondo et al., 2024]. However, none of them used all available stations between 40°S and 56°S and an updated model for crustal corrections [Mark et al., 2022].

Here we use the data-adaptive, multiscale tomographic approach of Hung et al. [2011] and relative sensitivity kernels to combine asynchronous datasets from several different temporary deployments [Maupin 2021] to map the 3-dimensional structure of the Patagonia slab window. As shown by Hung et al. (2011), the multiscale scheme brings improved precision in well-resolved regions. The new P and SH seismic velocity models yield broad regional coverage and extend to greater depths than Rayleigh wave models, which are limited to the upper 150-200 km. We provide new constraints on the present-day state of the mantle and how it contributes to back-arc magmatism. We also provide additional constraints on the manner in which earth structure contributes to the fast crustal uplift beneath the Patagonia icefields.

2. Data and methods

2.1. Broadband seismic data and processing

The dataset for this study (**Figure 1**) consists of seismograms from the GUANACO network of 26 broadband seismographs deployed from 2018-2021 [Wiens and Magnani, 2018], as well as previous deployments in the Chile triple junction region [Russo et al, 2010; Miller et al, 2023]. Additionally, we use 22 permanent stations from the Chile Seismic Network [Barrientos and CSN team, 2018] and the station PLCA from the global network [Albuquerque Seismological Laboratory (ASL)/USGS, 1993]. We analyzed three component seismic waveforms from teleseismic events between 28° and 98° of epicentral distance and magnitudes greater than 5.4 (**Figure S1a**).

Body wave travel-time delays are frequency dependent [Hung et al. 2004; Hung et al.; 2011; Kolstrup and Maupin 2015]. To account for this, we measure direct *P* and *SH wave* travel-times on waveforms band-pass-filtered around the secondary seismic noise peak (~0.2 Hz). We use

two frequency bands for P-waves (0.03-0.125 Hz and 0.3-1.5 Hz) and one frequency band for S-waves (0.03-0.125 Hz). Relative travel-times in different frequency bands are estimated from an automated processing procedure [Kolstrup and Maupin,2015] combining an iterative cross-correlation and stack algorithm (ICCS) [Lou et al., 2013] and the multichannel cross-correlation method [Van Decar and Crosson, 1990].

Data are corrected for crustal delay times using the crustal model from Mark et al. (2022) (**Figure S2**). To ensure a common reference time and include the effect of the topography, the crustal corrections are computed at each station by considering a model from 50 km below sea level and up to the free surface. In regions of thick sediments, reverberations and their interference introduce a significant frequency dependence of the travel-times measured on band-passed waveforms [Yang and Shen, 2006; Ritsema et al., 2009; Kolstrup and Maupin, 2015]. The crustal correction of finite-frequency travel-time residuals should therefore be made frequency dependent. This is done here following the procedure of Kolstrup and Maupin (2015).

2.2. Finite frequency body wave tomography

To invert the relative travel-times to obtain seismic velocity anomalies, we use the 3-D Born-Fréchet kernels, which link the influence of velocity heterogeneities and finite frequency travel-time shifts [Dahlen et al., 2000; Hung et al. 2000; Schmandt and Humphreys, 2010; Maupin and Kolstrup, 2015]. The kernels are demeaned to form relative kernels to correct for the unevenness in space and time of the data distribution [Ben-Mansour and Maupin, 2025].

We use the data-adaptive, multiscale, finite-frequency tomography method of Hung et al (2011) to take advantage of the distribution of seismic stations and the azimuthal distribution of teleseismic events. The model is parameterized in terms of wavelet basis functions in 3-D, where the calculations assume an isotropic Earth. The model has 65x33 points in the horizontal plane with interspacing of 0.31^{o}. The model extends from 50 to 650km depth with a 37.5 km grid spacing, but shallower and deeper models have also been tested (**Figure S3**). The inversion includes station terms, but tests with different weights for those show that they do not significantly affect the inverted model. As damping acts on the wavelet coefficients, there is no norm or gradient damping, but an ideal preservation of the resolved elements in the model [Hung et al. 2011, Kolstrup et al. 2015]. The resulting models do not provide absolute velocities but only velocity anomalies relative to an unknown average 1-D model. The optimal models for

P and S are determined by selecting the models with the best compromise between model norm and variance on one side and data misfit reduction on the other side. The misfit reduction is high, well above 60% even for smooth models, and 88% and 86% for the chosen P and S models respectively (**Figure S4a**). The models resolutions are illustrated in **Figure S4b.**

3. Results

3.1. P and SH relative velocity models

The new finite-frequency P and SH models provide improved resolution and image the mantle down to 650 km**.** Overall, the new models show larger velocity contrasts (**Figure 2**) of up to 4% compared to previous results with amplitudes on the order of 2% [Portner et al. 2022; Kondo et al. 2024], but the tomographic inversion used here conserves amplitudes quite well compared to other methods, as shown by Hung et al. (2011). The major patterns of the P and SH models are similar, with the magnitude of the S wave anomalies larger than the P wave anomalies as expected. There are some differences between the P and SH models in the detailed structure of the anomalies. These differences could be due to the unequal effects of the compositional and thermal anomalies on P and S wave velocities. However, because these differences could alternatively result from differences in data volume, signal to noise ratio, and frequency content, we do not extensively describe and interpret these differences and reserve most of our interpretation to the larger patterns reflected in both P and SH models (**Figure 2**).

The most prominent anomaly is a large region of low velocities anomalies between 46^{o}S and 49^{o}S (**Figures 2 and 3**), centered beneath the Meseta del Lago Buenos Aires volcanic (MBAV) region [Guivel et al., 2006, Guest et al, 2024]. Recent surface wave [Mark et al. 2022] and body wave [Russo et al. 2010, Portner et al., 2020; Rodriguez et al., 2021; Miller et al. 2023; Kondo et al. 2024] seismic models have shown the presence of a similar anomaly in this region. Synthetics tests on the depth extension of this low velocity anomaly by Kondo et al. (2024) suggest a maximum depth of 250km. Here, both P and S wave models show it extending down to at least 400 km, where it is underlain by faster velocities in the P-wave model. The anomaly is truncated in the north by faster velocities likely associated with the subducting Nazca slab. To the east, the lateral extent of the anomaly is limited at shallower depths (< 200 km) by the lithospheric mantle of the Deseado Massif (**Figures 2 and 3**). The E-W cross section C-C’

suggests that this anomaly extends eastward beneath the Deseado Massif but the absence of seismic stations in Argentina limits the interpretation of anomalies in this part of the model.

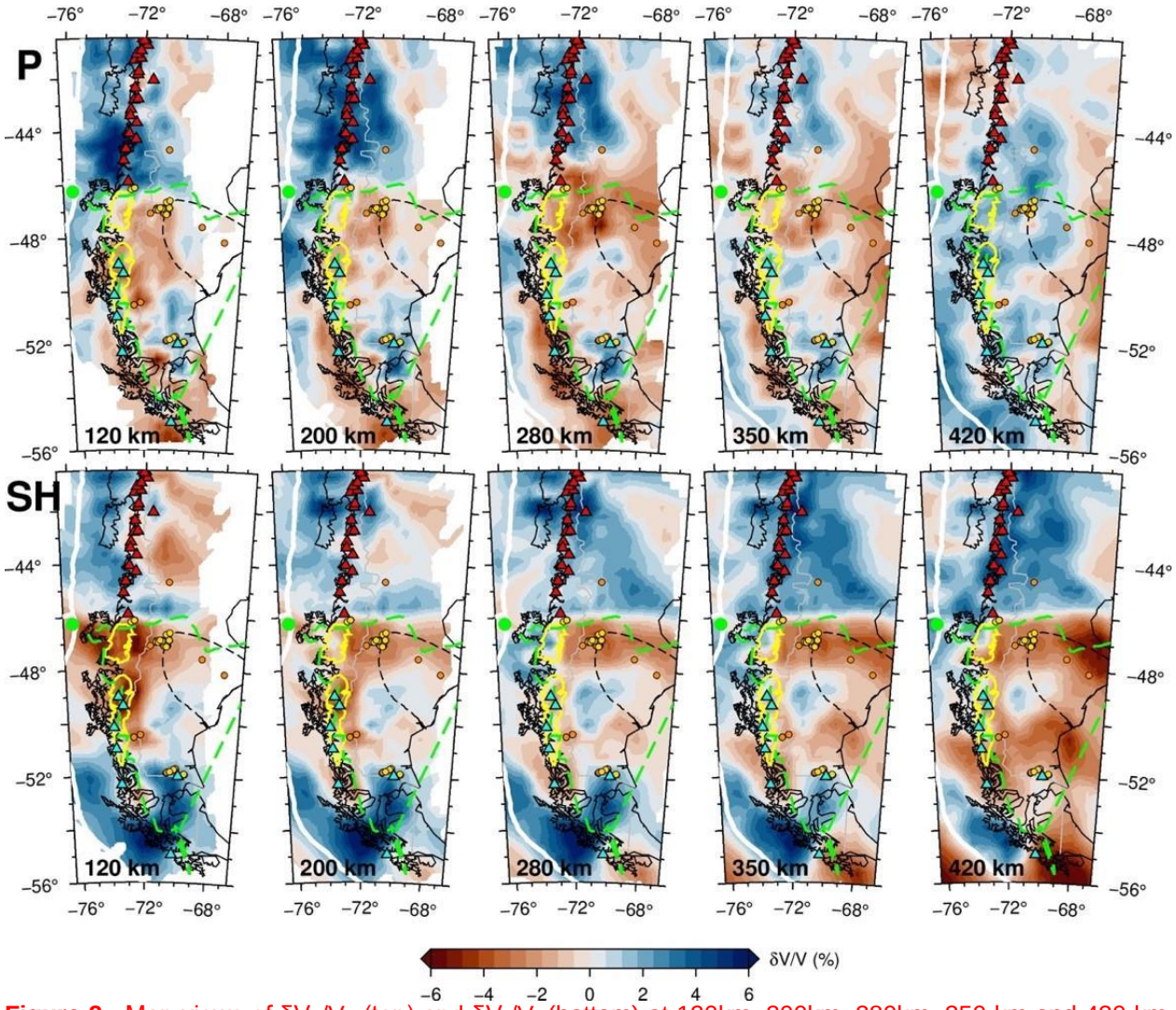

Figure 2. Map views of $\delta V_P/V_P$ (top) and $\delta V_S/V_S$ (bottom) at 120km, 200km, 280km, 350 km and 420 km depth. The dashed black line represents the surface extension of the Deseado Massif, green dashed line represents the maximum extension of the slab window and yellow contours are the location of the Northern and Southern Patagonia Icefield. The yellow/orange circles *represent young back-arc volcanism (<2Myrs) from Guillaume et al. (2010).* The green dot represents the location of the Chilean Triple Junction.

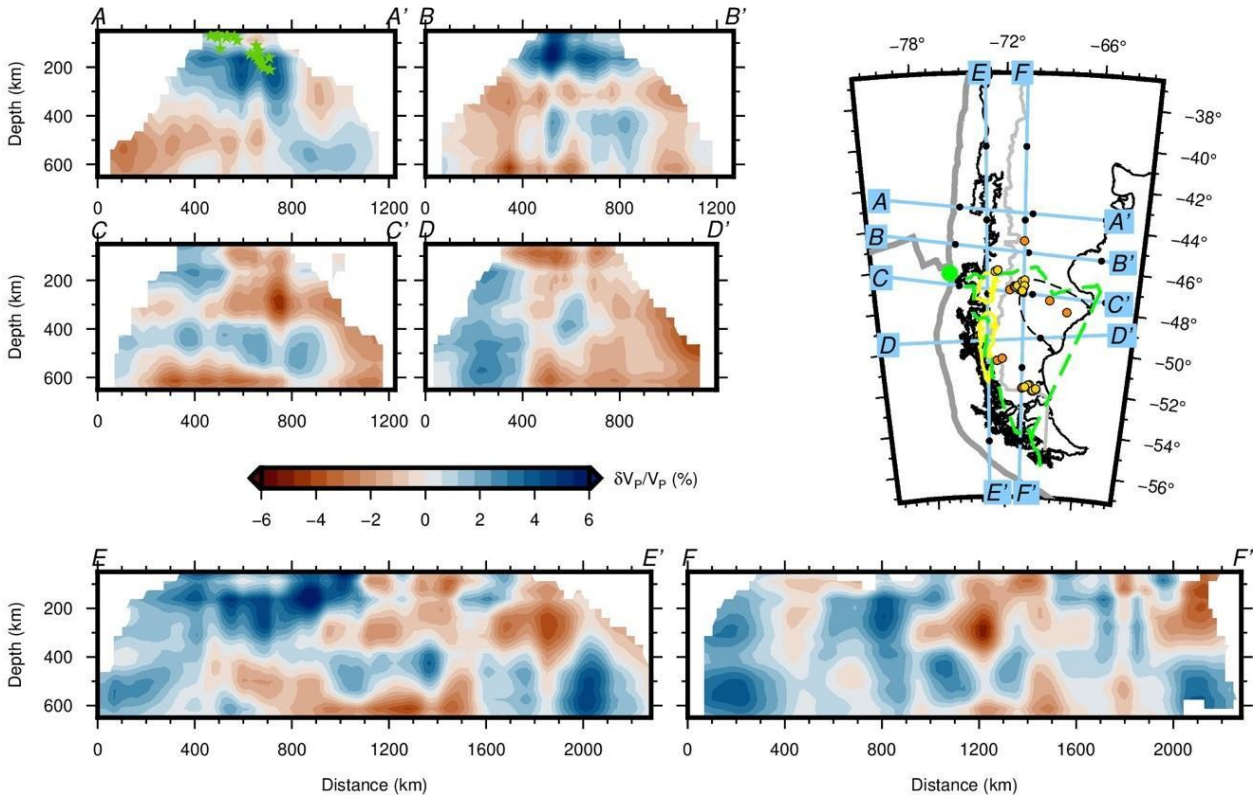

Figure 3. Cross-sections across P model. Green stars represent earthquakes from the US. Geological Survey catalogue (https://earthquake.usgs.gov/). The tectonic features on the map follow the same conventions as in Figure 2.

The northern part of the model region south to 46°S is dominated by fast seismic velocities likely associated with the subducting Nazca slab north of the triple junction. The E-W cross section A-A' in **Figure 3** suggests the presence of one anomaly following the Wadati-Benioff zone and then extending aseismically down to 350 km, and a deeper anomaly between 500-650 km beneath Argentina. Cross-section B-B' is very close to the slab edge, so the slab is not well resolved in this image. There is a clear contrast between a fast anomaly north of the CTJ and a low velocity anomaly in the south. This contrast matches the present-day location of the slab edge and the paleo-reconstruction of the Patagonia slab window by Breitsprecher and Thorkelson (2009) based on plate motion history. It also matches the boundary between a seismically active region to the North and a quiescent region to the South, where the absence of seismicity has been interpreted as the current locking of the subduction interface of the Antarctica slab [Ammirati et al., 2024] supported by geodetic observations [Richter et al., 2016] to the West.

The P model shows clearly that the fast relative velocity anomalies to the north of the CTJ (green dot on **Figure 2**) extends eastward and down to at least 350 km (**Figure S5**). Due to the nature of S waves and their frequency content, the SH model does not constrain the shape of the high anomaly as well.

3.2 Resolution tests

Checkerboard tests are used to evaluate the horizontal and vertical resolution in our datasets (**Figures S6-S8**). We test different sizes of checkers and velocity perturbations of +/- 4%. We add Gaussian noise to the synthetic data prior to inversion with standard deviation of 0.04 s and 0.14 s for P and S waves, respectively, as estimated from the actual data. The inversion is performed using the same parameters and damping as used with real data. The checkerboard tests show good recovery down to 420 km for both P waves (**Figures S6 and S7**) and SH waves (**Figures S6**). Tests also show that the P-wave datasets recover amplitudes better than the SH wave datasets.

In addition, we test several scenarios concerning the geometry and extension of the Nazca slab (**Figures S9-S11**), the lateral dimensions of the low velocity perturbation beneath 46^{o}S and 48^{o}S (**Figures S12, S13**), and the presence of two distinct shallow and deeper low velocity perturbations at the eastern edge of the study (**Figure S14**). Results suggest that (1) the Nazca slab has a gradual increase in slab dip with depth, and extends aseismically down to 350 km, (2) there is another velocity anomaly at about 550 km depth farther to the east (3) it is not clear whether there is a continuous slab, as the apparent connection between the anomalies in figure A-A' is not well resolved.

Tests on low velocity perturbations between 46^{o}S and 48^{o}S (**Figures S12-S14**) show a good recovery in P and SH velocities down to 420km and the ability to distinguish two distinct low velocity anomalies in this region.A comparison of our Vsh model with the Rayleigh wave Vsv model from Mark et al. (2022) (**Figures S15**) reveals relatively good agreement regarding the spatial distribution of fast and low velocity anomalies across the slab window in the depth range where both methods have good resolution.

4. Discussion

4.1. Low velocity mantle anomalies associated with back-arc volcanism

The tomographic models indicate an association between low velocity mantle anomalies and back-arc volcanism (**Figure 2**).

A strong low velocity mantle anomaly is located beneath the MBAV region, a locus of much of the Pleistocene back-arc volcanism (**Figure 1**). Continental back-arc volcanism is often assumed to occur by decompression melting from lithospheric extension, with shallow sources in the upper 100 km [Vasey et al, 2021]. Here, the low velocity seismic anomaly beneath the MBAV extends to depths of at least 400 km, indicating a deeper geodynamic process. In spite of the absence of seismic stations in eastern Argentine Patagonia, the E-W cross section C-C' (**Figure 3**) and resolution tests (**Figure S14**) suggest a connection eastward towards the Atlantic coast of the low velocity anomalies at depths greater than 250 km. The idea of mantle material coming from the Atlantic have been suggested in Patagonia [Soager et al, 2021; Guest et al, 2024] but is contrary to the typical assumption of a mantle flow from west to east [Russo et al, 2010; Hu et al, 2017; Ben Mansour et al, 2022]. Petrological and geochemical analyses of xenoliths from the lithospheric mantle support the idea of mantle heterogeneity inherited from South Atlantic hotspots (Discovery-Shona-Bouvet) [Soager et al. 2021; Mallick et al. 2023; Jalowitzki et al. 2024] prior to the opening of the Atlantic Ocean. In the absence of a plume (**Figure 3**), contamination of melts by the lithospheric mantle with Atlantic geochemical affinity provides an alternative explanation.

To the east at depths shallower than 200 km, the low velocity anomalies are truncated by the presence of the continental lithosphere supporting the Deseado Massif which borders the MBAV along its western boundary. The Deseado Massif is part of the Malvinas/Falkland Islands lithospheric block, a Precambrian terrain with strong mantle isotopic affinities with the Namaqua-Natal belt in south Africa [Marshall, 1994; Mundl et al., 2015; Schilling et al. 2017]. This lithospheric block is imaged farther to the south (~52^{o}-54^{o}S) with higher velocities in the upper 200 km, consistent with a thicker continental lithosphere (Mark et al, 2022, and **Figure 2**).

Between 50^{o}S and 52^{o}S, recent magmatism (< 2Myrs) has been recorded in the region of Cerro del Fraile [Guillaume et al., 2010]. This volcanism is located on the top of a low velocity anomaly in the shallow mantle (~ 120-160 km depth). Geochemical analysis of mantle xenoliths shows metasomatism of adakitic basalt, interpreted as the magmatic signature of the subduction of the current oceanic crust of the Antarctica Plate [Killian and Stern 2002; Stern 2004].

Interestingly, the Pali Aike volcanic field (PAV, **Figure 1**), with extensive Pleistocene and Holocene activity, is located on the interior of the Malvinas/Falkland lithospheric block [Shilling et al, 2017]. The origin of this volcanism is still debated. The occurrence of this volcanism in a region of thicker lithosphere, as imaged by high seismic velocities in the upper 200 km (**Figure 2**), demonstrates that back-arc volcanics can erupt even on the top of the interior of older lithospheric blocks, possibly aided by fractures or gaps in the lithosphere that are too small to image in this study.

4.2. The geometry of the aseismic southernmost Nazca slab

The present-day geometry of the southern edge of the Nazca slab is poorly constrained. Intermediate-depth earthquake hypocenters extend to depths of about 150 km. The depth extent of seismicity is limited by warm slab temperatures due to the slab's young lithospheric age, which is 7 Ma at the 45^{o}S trench axis and increases northward [Tebbens et al, 1997]. Breitsprecher and Thorkelson (2009) estimated the position of the slab edge using plate reconstructions and assuming a poorly constrained shallow dip angle. In their study, Portner et al. (2020) propose a new Nazca slab model with an aseismic extension down to ~300 km in this region (**Figure 1**).

Our P-wave tomographic model shows that the slab dip increases substantially at depths of 150-200 km, following the Wadati-Benioff zone. Our model also suggests the presence of stagnant slab at about 550 km depth (**Figure 3**). The presence of a fast velocity anomaly at about 550 km depth has been also observed in previous body wave models [Li et al. 2008; Lu et al. 2019] at these latitudes. From the comparison between geochemical signature of back arc magmatism and existing seismic models, Aragon et al. (2011) argue that the magmatism is generated by decompression melting from a stagnant detached Farallon slab. A slab gap has also been proposed between 350 km and 550 km in several global scale seismic models. However, in spite of new seismic stations deployed and used in this study, our structural tests (**Figure S10 and S11**) show poor depth sensitivity in this region, and fail to determine whether there is a slab gap or not.

4.3. Rheological heterogeneity beneath the Patagonia icefields

The NPI and SPI are located on top of the slab window between 46°S and 51°S. Their ice mass has been responding very sensitively to changing climate and atmospheric circulation. Changes of the ice load drive a delayed bedrock deformation due to glacial isostatic adjustment (GIA). According to GIA models [Ivins and James 2004; Dietrich et al. 2010; Lange et al. 2014], a homogeneous viscoelastic half space responds to an ice-mass loss with an elliptical geographic pattern through a) uplift with a concentrical pattern about the barycenter of the lost ice mass, and b) a symmetrical horizontal extension radially away from that barycenter. The effect of a reduced mantle viscosity of that half space is that the new isostatic equilibrium be restored in a shorter time, implying larger deformation rates [Weerdesteijn et al, 2022]. A localized low-viscosity anomaly, eccentrical with respect to the ice-load symmetry, enhances the horizontal deformation rates in the direction from the load center towards that anomaly [Kaufmann et al. 2005; Klemann et al. 2007].

GNSS observations in the SPI area reveal intense uplift, with rates reaching 4 cm/year in the northern part of the SPI, consistent with a GIA model assuming a homogeneous half space [Dietrich et al. 2010; Lange et al. 2014; Richter et al. 2016]. However, the observed uplift rates are smaller than the modelled ones in the southern part of SPI, south of 50°S, and larger than predicted by the simple GIA model in the northern part of SPI. Furthermore, the observed horizontal deformation is not symmetric about the N-S axis of the icefields, with a stronger eastward extension to the east of the load center compared to the westward extension to the west (see **Figure 4a** in Richter et al. 2016).

Seismic models offer an opportunity to estimate lateral changes in mantle viscosity, since both velocity and viscosity are largely controlled by temperature [Ivins et al, 2023]. However, recent detailed Rayleigh wave seismic structure models for southern Patagonia are limited to depths of about 150 km [Mark et al, 2022], whereas Irvins and James (2004) demonstrate the sensitivity of GIA effects on the asthenospheric thickness. The new models presented here can extend our understanding of rheological variations in this region to deeper depths and can thus provide explanations for the discrepancies between the observed deformation patterns and those predicted by GIA models based on a homogeneous rheology. The new seismic models show the NPI and the northern part of the SPI underlain by low velocities over most of the upper 300 km (**Figure 4**), indicating a thick zone of low viscosity asthenosphere in these regions.
Our seismic models also show a north-south dichotomy with the NPI and the northern part of the SPI underlain by low velocities and the southern SPI underlain by high velocities. This

dichotomy explains the increase from South to North of the observed uplift compared to the homogeneous model [Richter et al. 2016; Russo et al. 2022], as a consequence of the decrease in mantle viscosity in that direction, provided that the GIA model assumes a correct ice-load distribution. The presence of a very strong low-velocity anomaly in the back-arc near both icefields at 120 km depth, and for the NPI at deeper depths can explain the asymmetric horizontal deformation pattern as a modulation of the GIA-driven radial extension by a localized, low viscosity just east of the ice-load axis [Klemann et al. 2007].

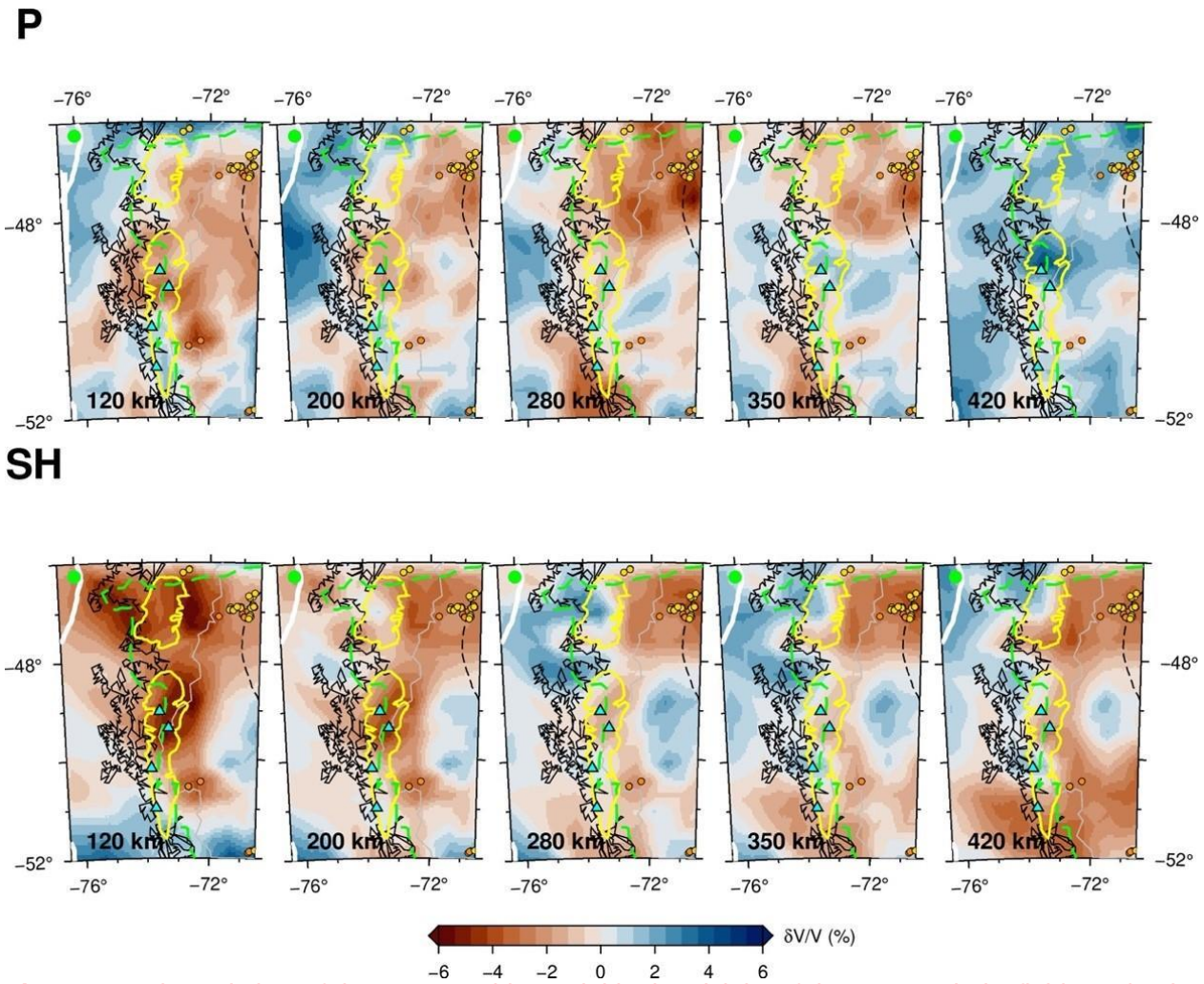

Figure 4. *Enlarged view of the tomographic model in the vicinity of the Patagonia icefields at depths of 120km, 200km, 280km, 350 km and 420km. The tectonic features on the map follow the same conventions as in Figure 2.*

5. Conclusions

We present new regional scale finite-frequency P and SH waves tomography models of southern Patagonia, using a wavelet-based multiscale parameterization that increases the recovery of amplitude and location of seismic velocity anomalies. The new models show a fast velocity anomaly north of the CTJ associated with the aseismic southernmost Nazca slab and a low velocity anomaly in southern Patagonia related to the present-day location of the slab window. We find that low velocity anomalies beneath back-arc volcanoes in the northern part of the slab window extend to depths of ~ 400 km, suggesting that the volcanism does not result from shallow mantle processes but is instead linked to upwelling thermal anomalies from deeper regions of the upper mantle. We also show that the southern edge of the Nazca slab extends downward to at least 350 km. Finally, the new tomographic models illuminate the structural heterogeneity beneath the Patagonia icefields. Our models show a north-south dichotomy, with the NPI and the northern part of the SPI underlain by low velocities and the southern SPI underlain by faster velocities down to depths of about 300 km. Very strong low-velocity anomalies in the back-arc near both icefields suggest that more complex rheological models may be able to explain geodetic observations in Patagonia.

Open Research

Data used in this study are from the temporary seismic networks GUANACO, SEARCH and CRSP temporary seismic networks respectively under the network code 1P, YJ and XJ. Permanents stations from the Chile network and Global network are under the network code C/C1 and GT. Data can be obtained from the EarthScope data center:

1P : https://www.fdsn.org/networks/detail/1P_2018/,

XJ: https://www.fdsn.org/networks/detail/XJ_2004/,

YJ: https://www.fdsn.org/networks/detail/YJ_2004/,

C: https://www.fdsn.org/networks/detail/C/,

C1: https://www.fdsn.org/networks/detail/C1/

GT: https://www.fdsn.org/networks/detail/GT/).

Tomography models showed and discussed in this study can be found in Ben-Mansour and Maupin (2025).

Acknowledgements

The authors thank the editor and two anonymous reviewers for the constructive comments that helped to improve this work. They also thank Celeste Bollini, Gerardo Connon, Leticia Duca, Nora Sabbione, Patrick Shore, Gerd Sielfeld, Daniel Valladares, Martin Vazquez, and many others for their work in planning, deploying, servicing and recovering the GUANACO seismic array. Finally, the authors would like to thank Erik Ivins and Alberto Saal for fruitful discussion in the early stage of the manuscript. The computations have been made using a modified version of the software for finite-frequency body wave tomography kindly provided by Shu-Huei Huang, National Taiwan University. Waveforms and metadata were accessed via the EarthScope Data Management System. This research was funded by the National Science Foundation under grant EAR-1714154: Collaborative Research: Solid Earth Response of the Patagonian Andes to Post-Little Ice Age Glacial Retreat. VM is supported by the Research Council of Norway's project 332523 (Center for Planetary Habitability). Figures were produced using GMT software [Wessel et al., 2013] using perceptually uniform colour maps generated by Fabio Crameri [Crameri, 2018].

References

Albuquerque Seismological Laboratory (ASL)/USGS. (1993). Global Telemetered Seismograph Network (USAF/USGS) [Dataset]. International Federation of Digital Seismograph Networks. https://doi.org/10.7914/SN/GT.

Ammirati, JB, Azua, K, Pasten-Araya, F, Richter, A, Wiens, DA, Flores, MC, Ruiz, S, Guzman-Marin, P, Lanza, F, Sielfeld, G (2024), Fault reactivation linked to rapid ice-mass removal from the Southern Patagonian Icefield (48--52° S), Tectonophysics, 230320.

Aragon, E, D'Eramo, F, Castro, A, Pinotti, L, Brunelli, D, Rabbia, O, Rivalenti, G, Varela, R, Spakman, W, Demartis, M, Cavarozzi, CE, Aguilera, YE, Mazzucchelli, M, Robot, A (2011), Tectono-magmatic response to major convergence changes in the North Patagonian suprasubduction system; the Paleogene subduction--transcurrent plate margin transition, Tectonophysics, 509,3-4, 218--237.

Barrientos, S, National Seismological Center (CSN) Team (2018), The Seismic Network of Chile. Seismological Research Letters, 89, 2A, 467-474.

Ben-Mansour, W, Wiens, DA, Mark, HF, Russo, RM, Richter, A, Marderwald, E, Barrientos, S (2022), Mantle flow pattern associated with the Patagonian slab window determined from azimuthal anisotropy, Geophysical Research Letters, 49,18, e2022GL099871.

Ben-Mansour, W, Maupin, V (2025), Optimizing data usage in regional body wave tomography by using asynchronous network data and relative sensitivity kernels: an example from Patagonia, EarthArXiv, https://doi.org/10.31223/X5WB2P.

Ben-Mansour, W, Maupin, V (2025), Deep source regions for Patagonia back-arc volcanism imaged by finite frequency body wave tomography [Dataset & Software]. Zenodo. https://doi.org/**10.5281/zenodo.10028616**

Breitsprecher, K, Thorkelson, DJ (2009), Neogene kinematic history of Nazca-Antarctic - Phoenix slab windows beneath Patagonia and the Antarctic Peninsula, Tectonophysics, 464 , 1-4 ,10-20.

Crameri, F (2018). Scientific colour-maps: perceptually uniform and colour blind friendly, www.fabiocrameri.ch/colourmaps.

Dahlen, FA and Hung, S-H and Nolet, Guust (2000), Frechet kernels for finite-frequency traveltimes: I. Theory, Geophysical Journal International,141,1,157-174.

Dietrich, R, Ivins, ER, Casassa, G , Lange, H , Wendt, J , Fritsche, M (2010), Rapid crustal uplift in Patagonia due to enhanced ice loss, Earth and Planetary Science Letters,2898, 1-2,22-29.

Gorring, ML, Kay, SM, Zeitler, PK, Ramos, VA, Rubiolo, D, Fernandez, MI, Panza, JL (1997), Neogene Patagonian plateau lavas: continental magmas associated with ridge collision at the Chile Triple Junction,Tectonics,16,1,1--17.

Gorring, M, Singer, B, Gowers, J, Kay, Suzanne M (2003), Plio--Pleistocene basalts from the Meseta del Lago Buenos Aires, Argentina: evidence for asthenosphere--lithosphere interactions during slab window magmatism, Chemical Geology, 193, 3-4, 215-235.

Groome, WG and Thorkelson, DJ (2009), The three-dimensional thermo-mechanical signature of ridge subduction and slab window migration, Tectonophysiccs,464,1-4, 70-83.

Guest, IA, Saal, AE, Mallick, S, Gorring, ML, Kay, SM (2024), The volcanism of the Meseta del Lago Buenos Aires, Patagonia: the transition from subduction to slab window, Journal of Petrology, 65 ,6.

Guillaume, B, Moroni, M, Funiciello, F, Martinod, J, Faccenna, C (2010), Mantle flow and dynamic topography associated with slab window opening: Insights from laboratory models, Tectonophysics, 496,1—4,83—98.

Guivel, C, Morata, D, Pelleter, E, Espinoza, F, Maury, RC, Lagabrielle, Y, Polve M, Bellon, H, Cotten, J, Benoit, M, SUarez, M, De la Cruz, R (2006), Miocene to Late Quaternary Patagonian basalts (46--47 S): geochronometric and geochemical evidence for slab tearing due to active spreading ridge subduction, Journal of Volcanology and Geothermal Research, 149, 3-4, 346--370.

Hu, Jiashun and Faccenda, Manuele and Liu, Lijun (2017), Subduction-controlled mantle flow and seismic anisotropy in South America, Earth and Planetary Science Letters, 470, 13-24.

Hung, S-H and Dahlen, FA and Nolet, Guust (2000), Frechet kernels for finite-frequency traveltimes: II. Examples, Geophysical Journal International, 141, 1,175-203.

Hung, SH, Chen, WP, Chiao, LY (2011), A data-adaptive, multiscale approach of finite-frequency, traveltime tomography with special reference to P and S wave data from central Tibet,Journal of Geophysical Research: Solid Earth, 116, B6.

Ivins, ER and James, TS (2004), Bedrock response to Llanquihue Holocene and present-day glaciation in southernmost South America, Geophysical Research Letters, 31,24.

Ivins, E. R., W. van der Wal, D. A. Wiens, A. J. Lloyd, and L. Caron (2023). Antarctic upper mantle rheology, *The Geochemistry and Geophysics of the Antarctic Mantle*, Geological Society, London, Memoirs, 56, 267-294.

Jalowitzki, T, Sumino, H, Conceicao, RV, Schilling, ME, Bertotto, GW, Tassara, A, Gervasoni, F, Orihashi, Y, Nagao, K, Rocha, MP, Antonio de Freitas Rodrigues R (2024), Pristine helium from the Karoo mantle plume within the shallow asthenosphere beneath Patagonia, Nature Communications, 15,1, 6402.

Kaufmann, G, Wu, P, Ivins, ER (2005), Lateral viscosity variations beneath Antarctica and their implications on regional rebound motions and seismotectonics, Journal of Geodynamics, 39, 2, 165-181.

Kilian, R and Stern, CR (2002), Constraints on the interaction between slab melts and the mantle wedge from adakitic glass in peridotite xenoliths, European Journal of Mineralogy,14,1, 25-36.

Klemann, V., Ivins, E., Martinec, Z., Wolf, D. (2007). Models of active glacial isostasy roofing warm subduction: case of the South Patagonian Ice field, Journal of Geophysical Research: Solid Earth, 112, B09405.

Kolstrup, ML, Hung, SH, Maupin, V (2015), Multiscale, finite-frequency P and S tomography of the upper mantle in the southwestern Fennoscandian Shield, Geophysical Journal International, 202, 1, 190-218.

Kondo, Y, Obayashi, M, Sugioka, H, Shiobara, H, Ito, A, Shinohara, M, Iwamori, H, Kinoshita, M, Miller, M, Tassara, C, Ojeda, J (2024), Seismic image of the central to southern Andean subduction zone through finite-frequency tomography, Journal of Geophysical Research: Solid Earth, 129,11.

Lange, H, Casassa, G, Ivins, ER, Schroder, L, Fritsche, M, Richter, A, Groh, A, Dietrich, R (2014), Observed crustal uplift near the Southern Patagonian Icefield constrains improved viscoelastic Earth models, Geophysical Research Letters, 41, 3, 805-812.

Li, C, Van Der Hilst, RD, Engdahl, ER, Burdick, S (2008), A new global model for P wave speed variations in Earth's mantle, Geochemistry, Geophysics, Geosystems, 9, 5.

Lou, X, Van Der Lee, S, Lloyd, S (2023), AIMBAT: A python/matplotlib tool for measuring teleseismic arrival time, Seismological Research Letters, 84, 1, 85-93 .

Lu, C, Grand, SP, Lai, H, Garnero, EJ (2019), TX2019slab: A new P and S tomography model incorporating subducting slabs, Journal of Geophysical Research: Solid Earth, 124, 11, 11549--11567.

Mallick, S, Kuhl, SE, Saal, AE, Klein, EM, Bach, W, Monteleone, BD, Boesenberg, JS (2023), Evidence of South American lithosphere mantle beneath the Chile mid-ocean ridge, Earth and Planetary Science Letters, 620, 118320.

Mark, HF, Wiens, DA, Ivins, ER, Richter, A, Ben Mansour, W, Magnani, MB, Marderwald, E, Adaros, R, Barrientos, S(2022), Lithospheric erosion in the Patagonian slab window, and implications for glacial isostasy, Geophysical Research Letters, 49, 2, e2021GL096863.

Marshall, JEA (1994), The Falkland Islands: a key element in Gondwana paleogeography, Tectonics, 13, 2, 165-181.

Maupin, V, Kolstrup, ML (2015), Insights in P-and S-wave relative traveltime tomography from analysing finite-frequency Frechet kernels, Geophysical Journal 202, 3,1581-1598.

Maupin, V (2021), Combining asynchronous data sets in regional body-wave tomography, Geophysical Journal International, 224, 1, 401-415.

Miller, M, Priestley, K, Tilmann, F, Bataille, K, Iwamori, H (2023), P wave teleseismic tomography of the subducted Chile rise, Journal of South American Earth Sciences, 128, 104474.

Mundl, A, Ntaflos, T, Ackerman, L, Bizimis, M, Bjerg, EA., Hauzenberger, CA (2015), Mesoproterozoic and Paleoproterozoic subcontinental lithospheric mantle domains beneath southern Patagonia: Isotopic evidence for its connection to Africa and Antarctica, Geology, 43, 1, 39-42.

Portner, DE, Rodriguez, EE, Beck, S, Zandt, G, Scire, A, Rocha, MP, Bianchi, MB, Ruiz, M, Francca, GS, Condori, C, Alavadaro , P (2020), Detailed structure of the subducted Nazca slab

into the lower mantle derived from continent-scale teleseismic P wave tomography, Journal of Geophysical Research: Solid Earth, 125, 5.

Ramos, VA and Kay, SM (1992),Southern Patagonian plateau basalts and deformation: backarc testimony of ridge collisions, Tectonophysics,205, 1-3, 261--282.

Richter, A, Ivins, E, Lange, H, Mendoza, L, Schroder, L, Hormaechea, JL, Casassa, G, Marderwald, E, Fritsche, M, Perdomo, R, Horwath, M, Dietrich R (2016), Crustal deformation across the Southern Patagonian Icefield observed by GNSS, Earth and Planetary Science Letters, 52, 206-215.

Richter, A, Groh, A, Horwath, M, Ivins, E, Marderwald, E, Hormaechea, JL, Perdomo, R, Dietrich, R (2019), The rapid and steady mass loss of the Patagonian icefields ,throughout the GRACE era: 2002--2017, Remote Sensing,11,8,909.

Ritsema, J, Van Heijst, HJ, Woodhouse, JH, Deuss, A (2009), Long-period body wave traveltimes through the crust: implication for crustal corrections and seismic tomography, Geophysical Journal International, 179, 2, 1255-1261.

Rodriguez, EE, Portner, DE, Beck, SL, Rocha, MP, Bianchi, MB, Assumpccao, M, Ruiz, M, Alvarado, P, Condori, C, Lynner, C (2021), Mantle dynamics of the Andean Subduction Zone from continent-scale teleseismic S-wave tomography, Geophysical Journal International, 224, 3, 1553-1571.

Russo, RM (2010), Subduction of the Chile Ridge: Upper mantle structure and flow, Gsa Today, 20.

Russo, RM, Luo, H, Wang, K, Ambrosius, B, Mocanu, V, He, J, James, T, Bevis, M, Fernandes, R (2022), Lateral variation in slab window viscosity inferred from global navigation satellite system (GNSS)--observed uplift due to recent mass loss at Patagonia ice fields, Geology,50,1,111—115.

Sanhueza, J, Yanez, G, Buck, WR, Araya Vargas, J, Veloso, E (2023), Ridge subduction: Unraveling the consequences linked to a slab window development beneath South America at the Chile Triple Junction, Geochemistry, Geophysics, Geosystems,24,9,e2023GC010977.

Schilling, ME, Carlson, RW, Tassara, A, Conceiccao, RV, Bertotto, GW, Vasquez, M, Munoz, Daniel, Jalowitzki, T, Gervasoni, F, Morata, Di (2017), The origin of Patagonia revealed by Re-Os systematics of mantle xenoliths, Precambrian Research, 294, 15-32.

Schmandt, B and Humphreys, E (2010), Seismic heterogeneity and small-scale convection in the southern California upper mantle, Geochemistry, Geophysics, Geosystems,11,5.

Soager, N, Holm, PM, Massaferro, GI, Haller, M, Traun, M K (2021), The Patagonian intraplate basalts: A reflection of the South Atlantic convection cell, Gondwana Research , 91, 40-57.

Stern, CR (2004), Active Andean volcanism: its geologic and tectonic setting, Revista geologica de Chile,31,2, 161-206.

Tebbens, S. F., S. C. Cande, L. Kovacs, J. C. Parra, J. L. LaBrecque, and H. Vergara (1997), The Chile ridge: A tectonic framework, Journal of Geophysical Research: Solid Earth,102, B6, 12035–12059.

Thorkelson, DJ and Breitsprecher, K (2005), Partial melting of slab window margins: genesis of adakitic and non-adakitic magmas, Lithos, 79,1-2,25-41.

Van Decar, JC and Crosson, RS (1990), Determination of teleseismic relative phase arrival times using multi-channel cross-correlation and least squares, Bulletin of the Seismological Society of America, 80,1, 150-169.

Vasey, DA, Cowgill, E, Cooper, KM (2021), A preliminary framework for magmatism in modern continental back-arc basins and its application to the Triassic-Jurassic tectonic evolution of the Caucasus, Geochemistry, Geophysics, Geosystems, 22, 6.

Weerdesteijn, MFM, Conrad, CP, Naliboff, JB (2022), Solid Earth Uplift Due To Contemporary Ice Melt Above Low-Viscosity Regions of the Upper Mantle, Geophysical Research Letters, 49,17.

Wessel, P., Smith, W., Scharroo, R., Luis, J., Wobbe, F. (2013). Generic Mapping Tools: improved version released, EOS, Trans. Am. geophys. Un., 94, 409-410.

Wiens, DA and Magnani, MB (2018), Solid Earth response of the Patagonia Andes to post-Little Ice Age glacial retreat, International Federation of Digital Seismograph Networks. https://doi.org/10.7914/SN/1P_2018.

Yang, T and Shen, Y (2006), Frequency-dependent crustal correction for finite-frequency seismic tomography, Bulletin of the Seismological Society of America, 96, 6, 2441-2448.

Supplementary Materials: Deep source regions for back-arc volcanism in the Patagonian slab window imaged by finite frequency P and SH body wave tomography

Walid Ben-Mansour [(1)], Valerie Maupin[(2)], Douglas A Wiens[(1)], Andreas Richter[(3)],

(1) Department of Earth, Environmental and Planetary Sciences, Washington University in Saint Louis, Saint Louis, MO, USA, (2) University of Oslo, PHAB, Oslo, Norway, (3) Laboratorio, MAGGIA, Universidad Nacional de La Plata, CONICET, La Plata, Argentina

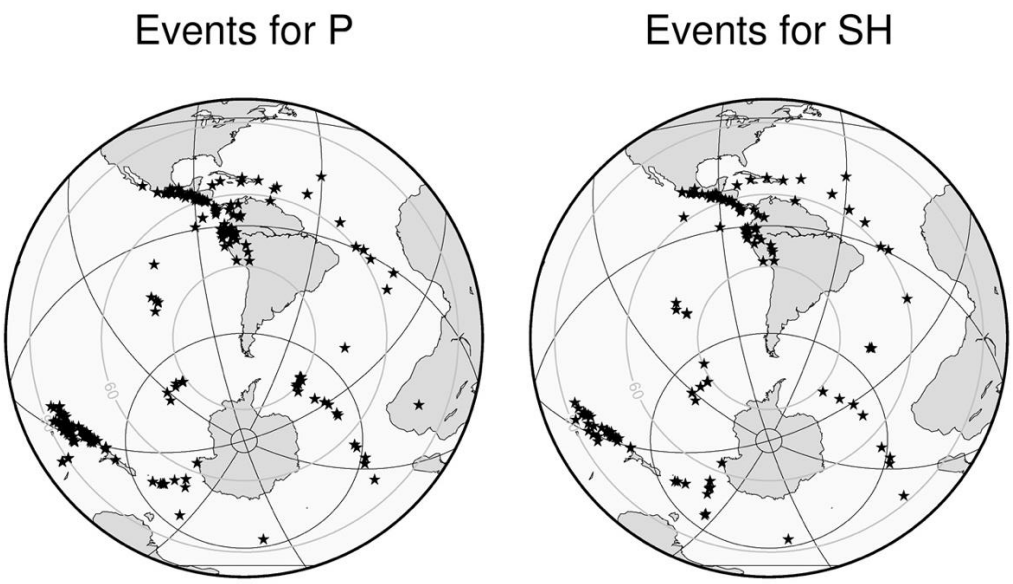

Figure S1. Teleseismic events used in the finite frequency body wave tomography for P and SH waves.

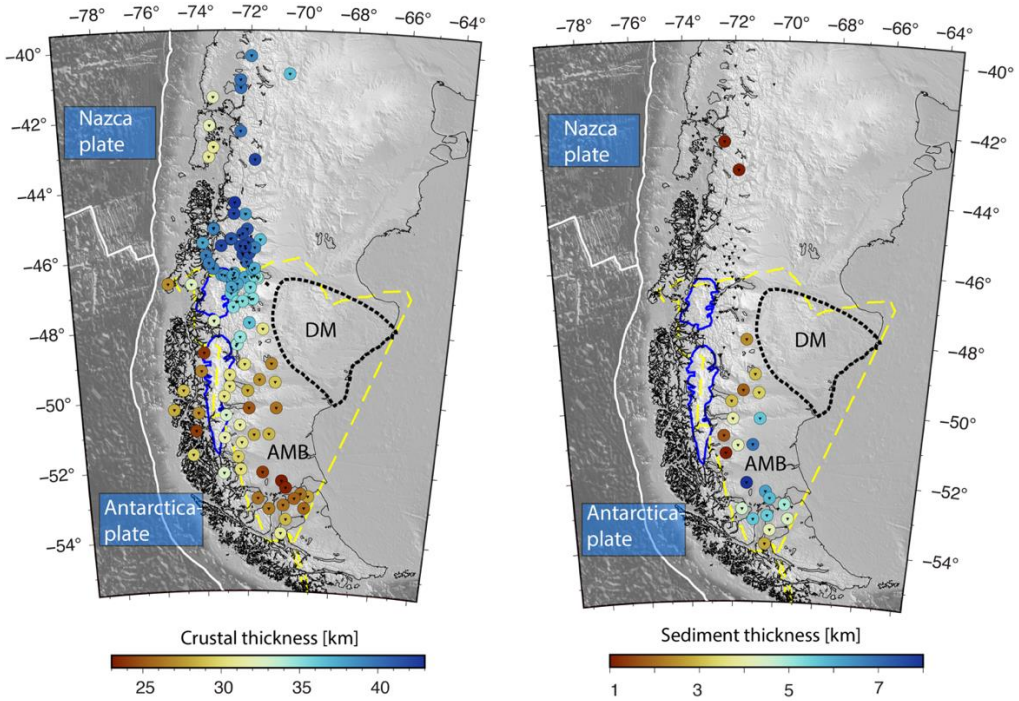

Figure S2a. Moho depth (left) and sediments thickness (right) from Mark et al. (2022) used for the crustal correction. DM: Deseado Massif, AMB: Austral Magallanes Basin. Yellow dashed lines represent the maximum extension of the slab window and blue contour the Patagonia icefield. Black triangles are the locations of seismic stations used in this study.

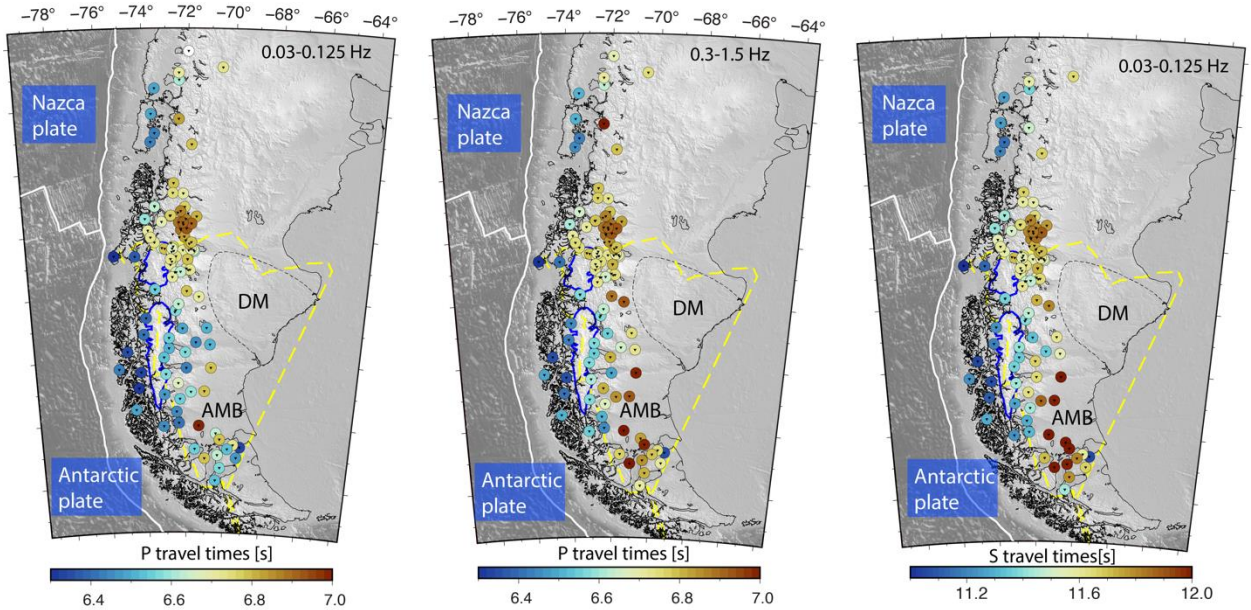

Figure S2b. Travel times from 50km below sea-level to the surface, including topography, for, from left to right, low-frequency P waves, high-frequency P waves and SH waves. Note the frequency dependence of the P-wave travel times in regions with thick sediments where low frequencies display reduced travel times.

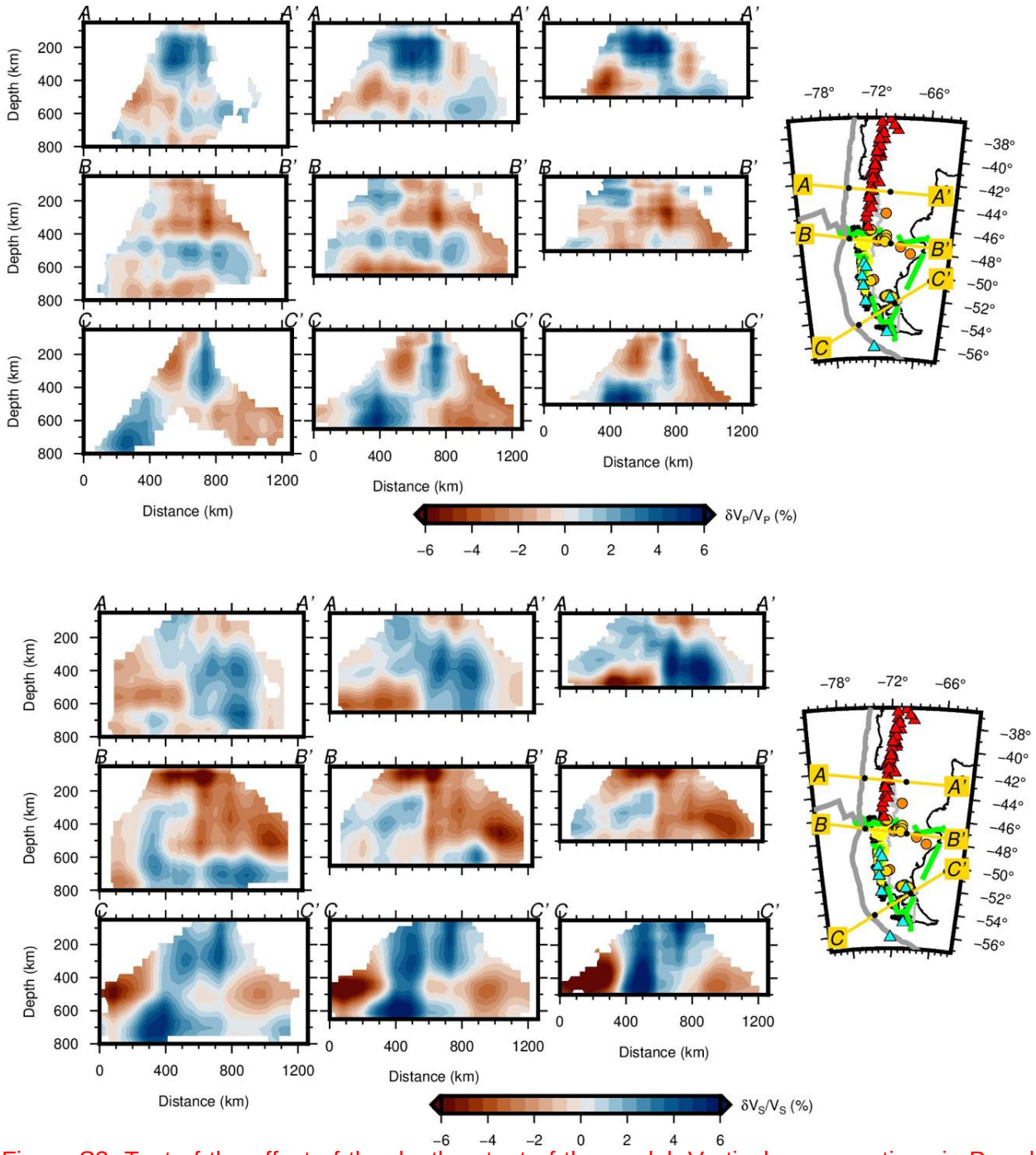

Figure S3. Test of the effect of the depth extent of the model. Vertical cross sections in P and SH models extending from left to right down to 800, 650 and 500km depth. The tectonic features on the map follow the same conventions as in Figure 2 in the manuscript. We observe that changing the depth extend of the model does not strongly modify the depth of the anomalies in the model.

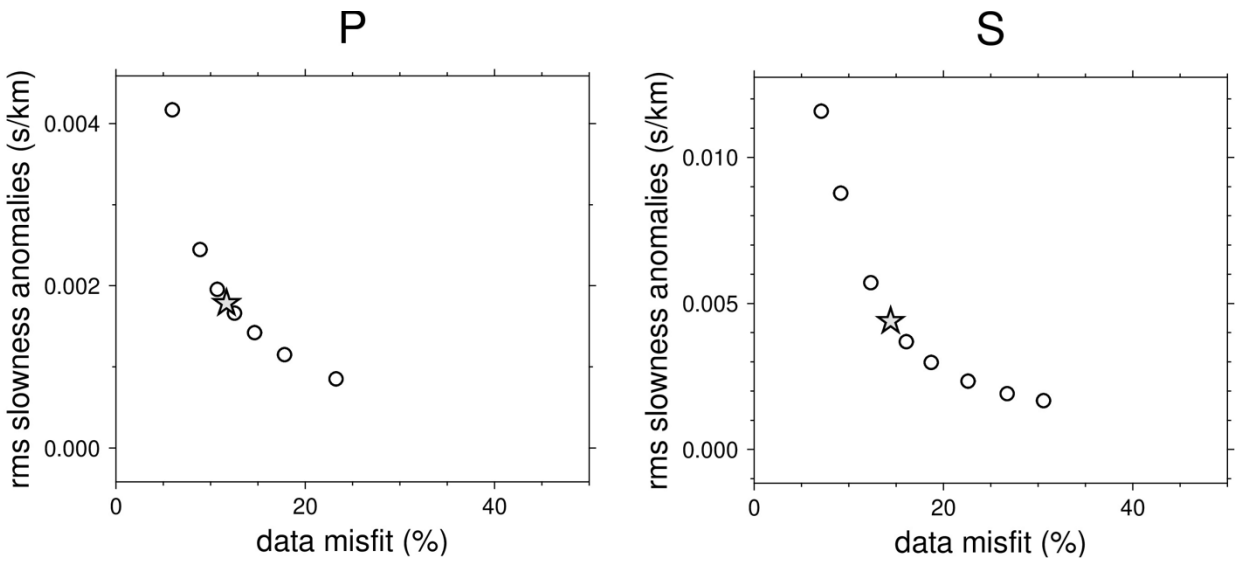

Figure S4a. Trade-off between rms of slowness anomalies and data misfit. The star represents the preferred solutions shown in the manuscript for P and SH. The data misfit is the sum of the squared differences between observed and predicted data, after being normalized by the sum of the squares of observed data. The different solutions correspond to different values of λ in equation 7 in Hung et al. (2011) and vary from 1000 to 30000 with a preferred value of 5000 for the P-wave tomography, and from 300 to 12000 with a preferred value of 1500 for the S-wave tomography.

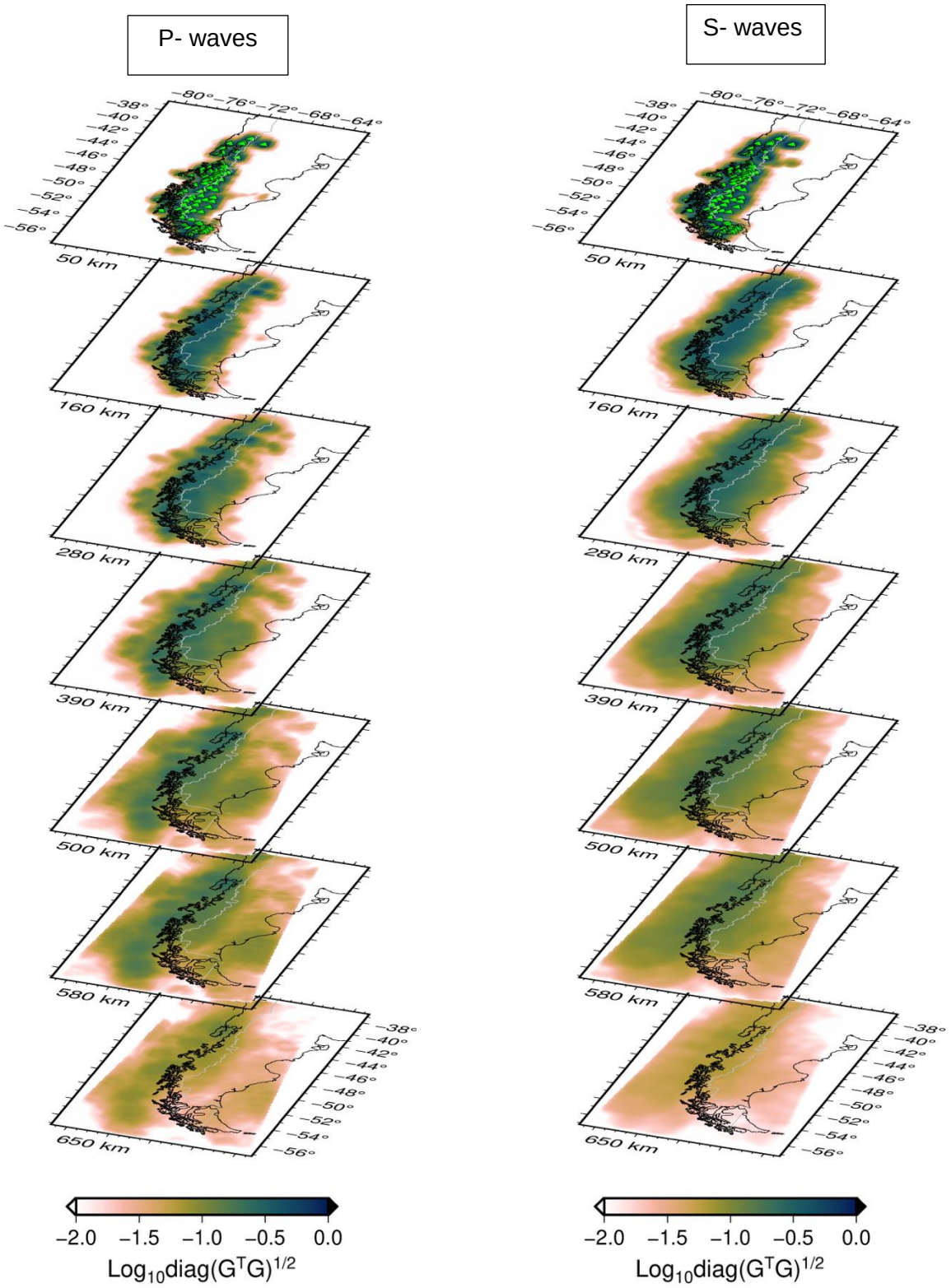

Figure S4b. Images of the value of the square-root of the diagonal elements of the G^TG matrix relative to its maximum value, as a proxy for the resolution matrix. Only values larger than 0.01 (log larger than -2.0) are shown. This also corresponds to the cut-off value used in all other figures to avoid plotting the models in unresolved regions.

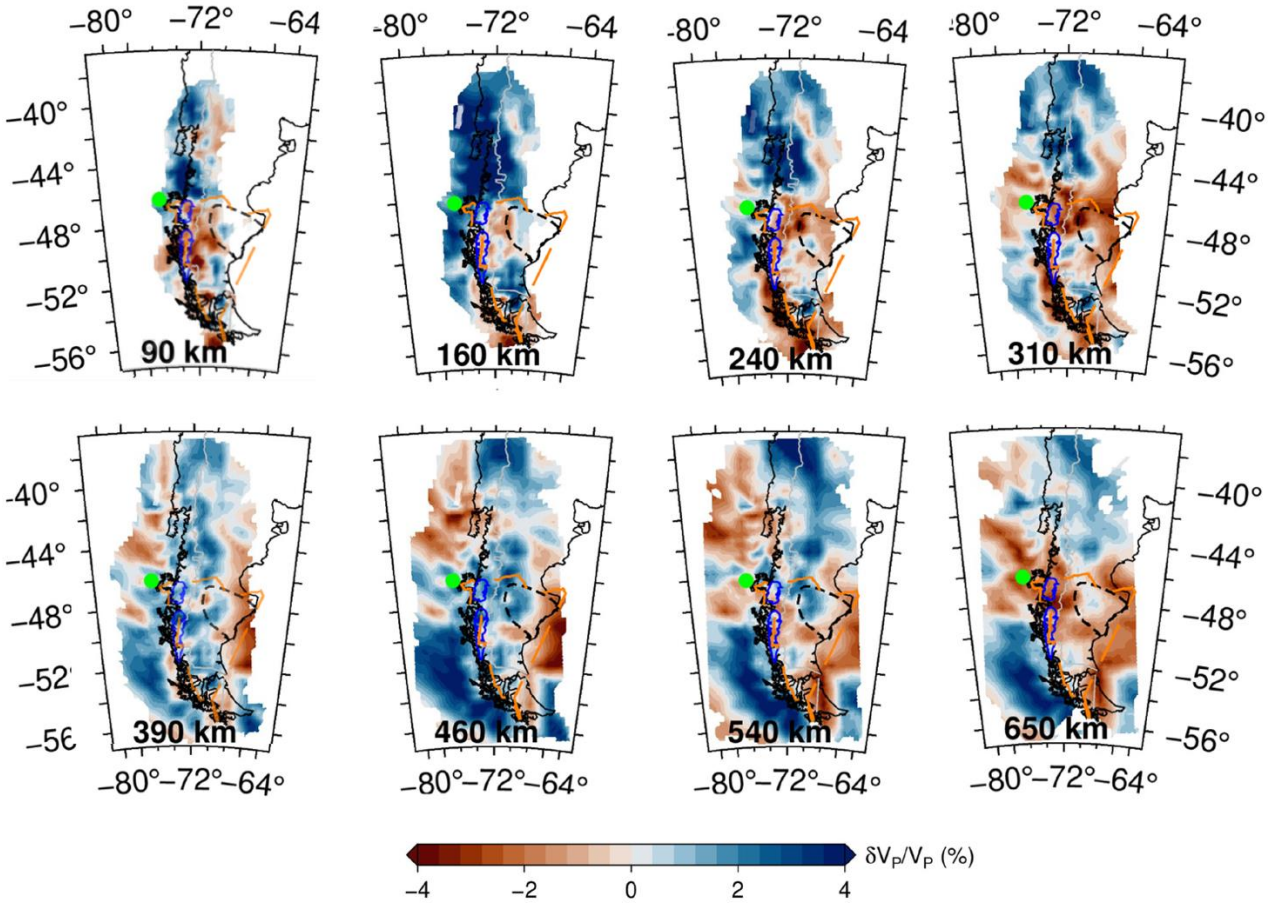

Figure S5. Map view of P model from eight slices from 90 to 650 km depth. The tectonic features on the map follow the same conventions as in Figure 2 in the manuscript.

Checkerboard tests

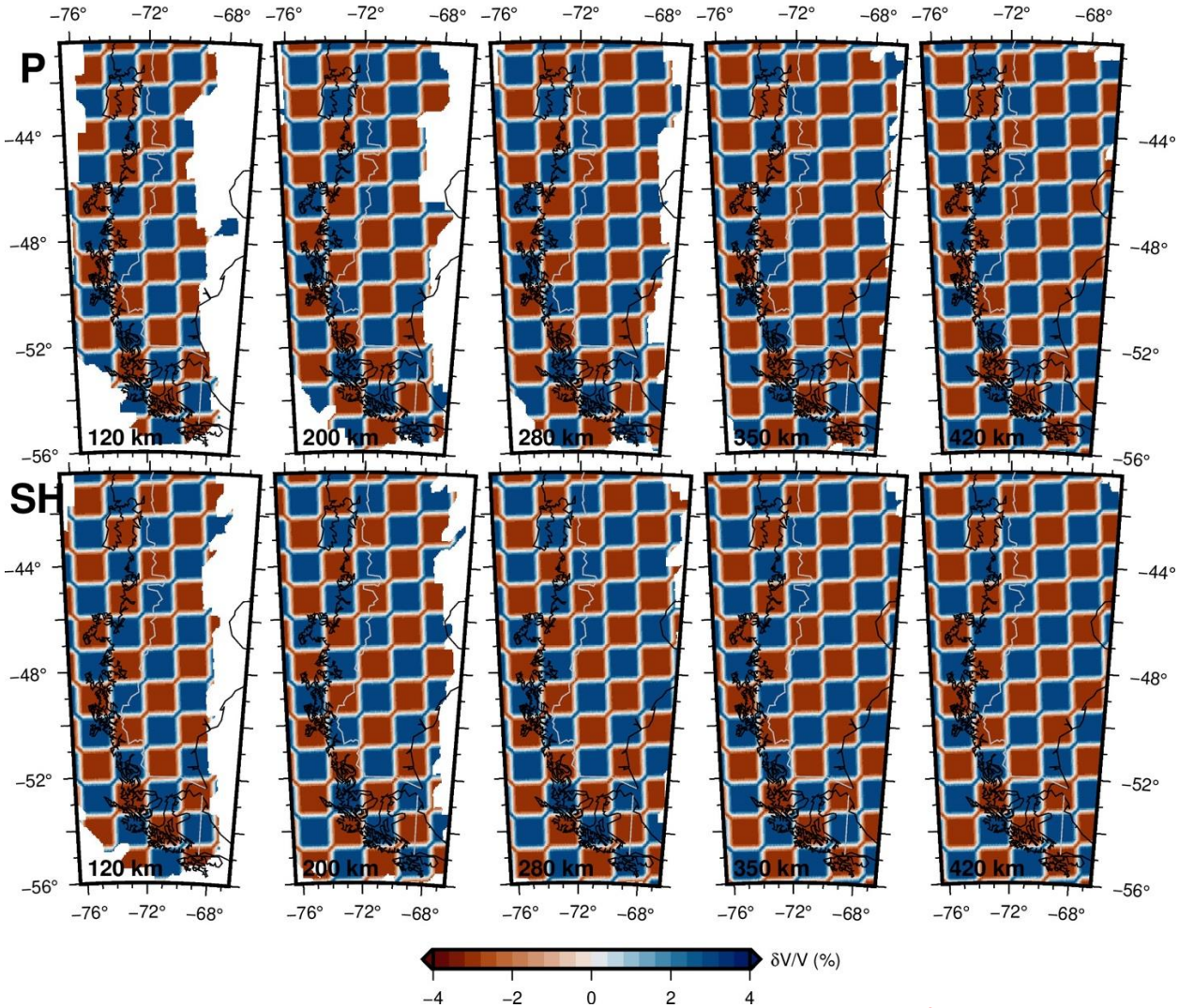

Figure S6a. Synthetic input model for a checkerboard test with cells of 1.25° in horizontal dimensions, 150km in vertical dimension, δlnV_P = ±4% (top), and δlnV_S = ±4 % (bottom). Maps at 120, 200, 280, 350 and 420 km depth.

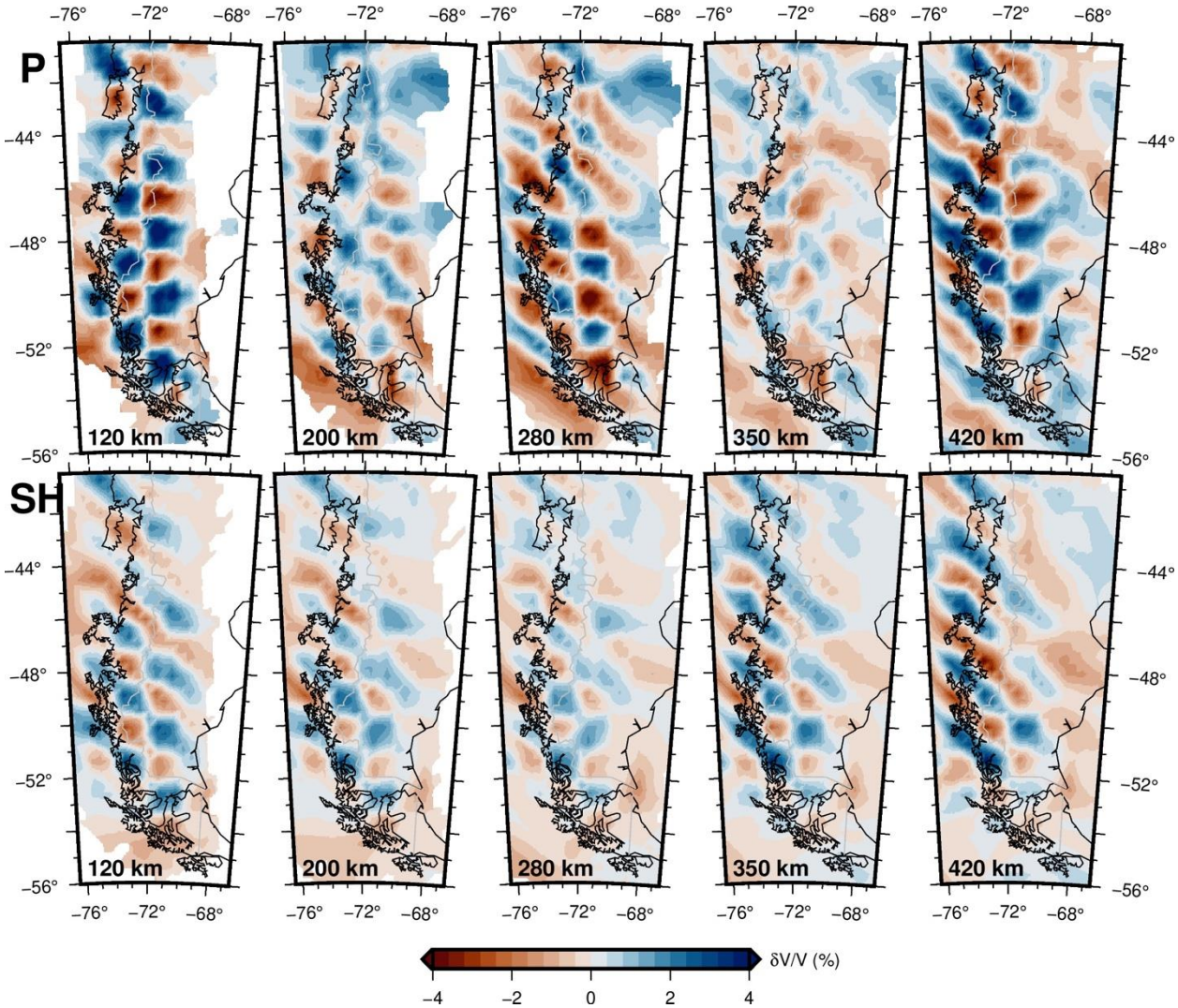

Figure S6b. Recovery for checkerboard tests presented in Figure S6a. The variation in the recovery of the amplitudes with depth suggests a slight shift of the anomalies towards larger depths for P waves, whereas the results for S waves show that the resolution at the scale of these cells is poor for these waves.

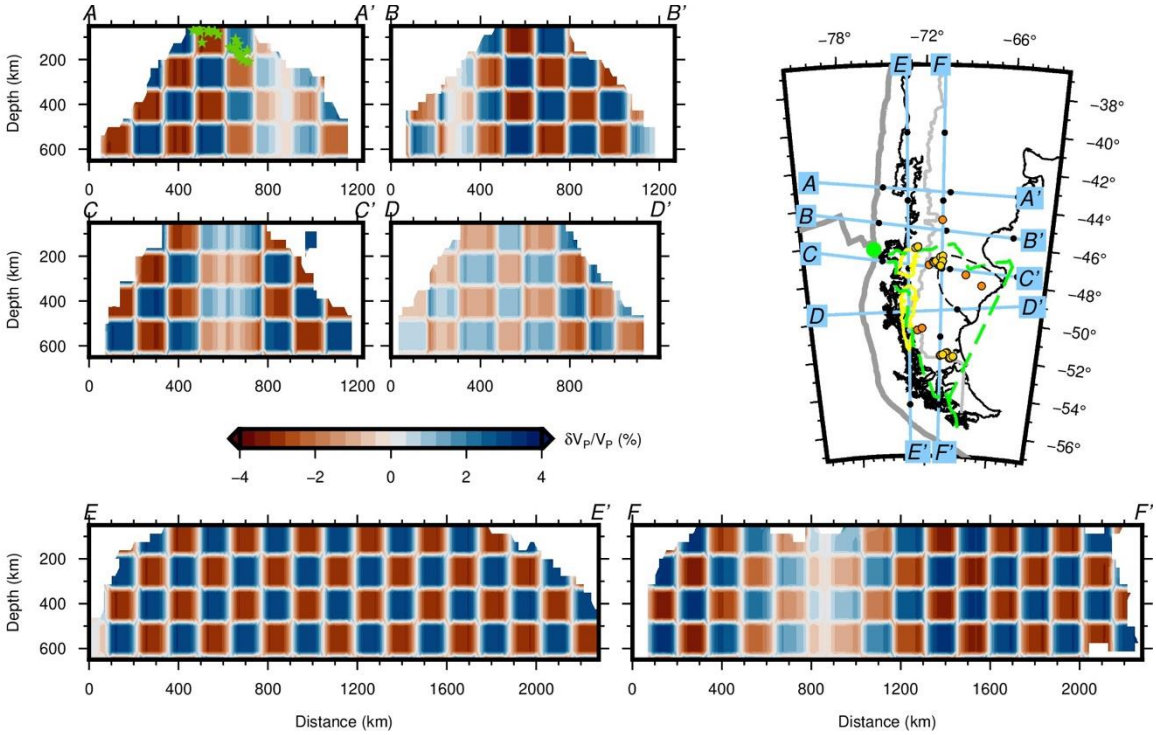

Figures S7a. Vertical cross-sections in the checkerboard synthetic model for P waves presented in Figure S6a. Map view of study area with the location of different profiles. The tectonic features on the map follow the same conventions as in Figure 2 in the manuscript.

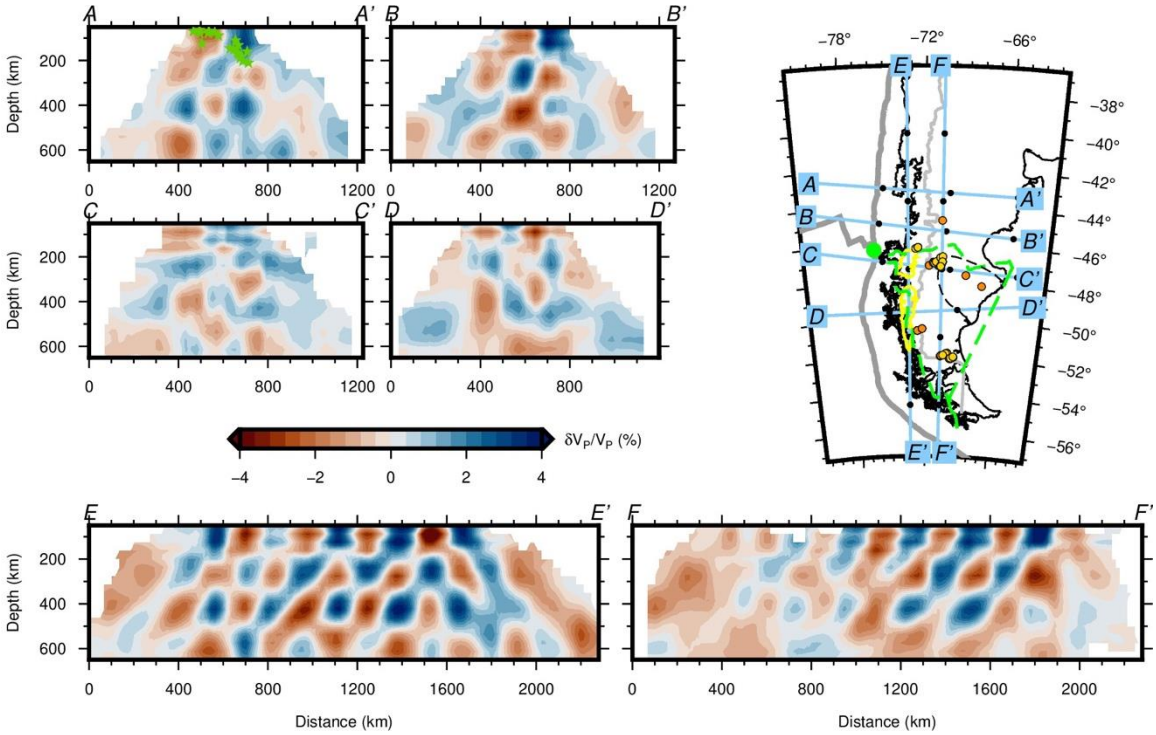

Figure S7b. Recovery for checkerboard test presented in Figure S7a.

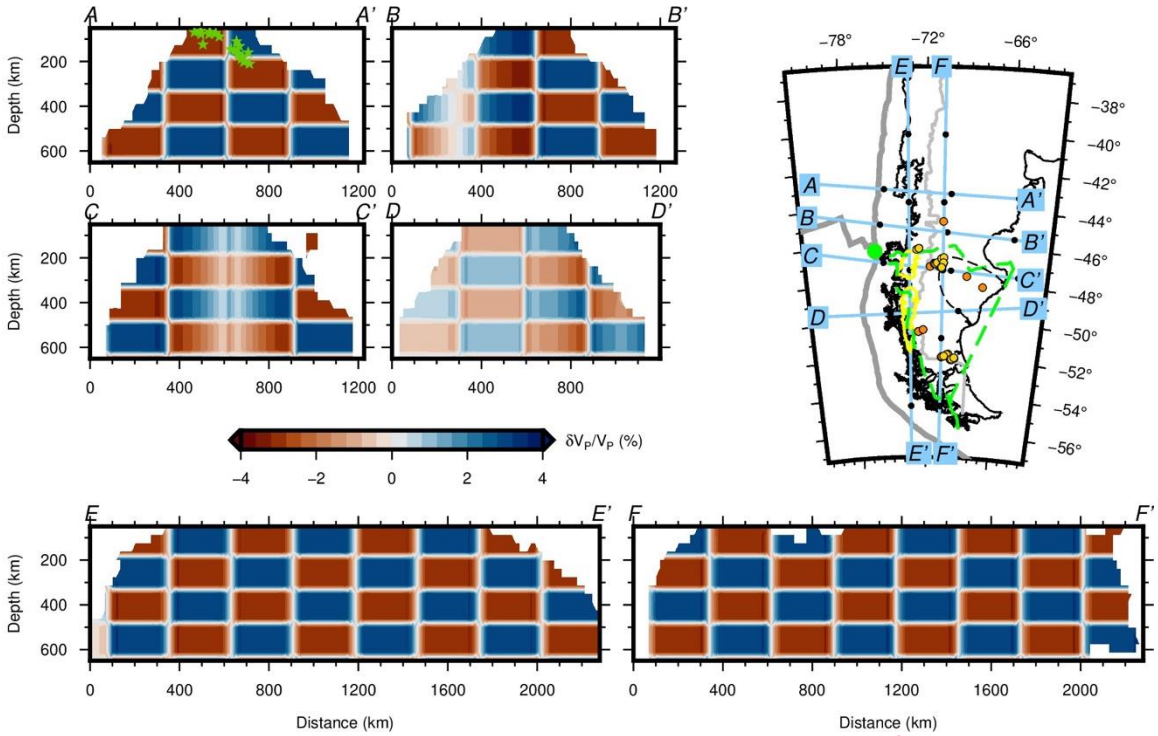

Figures S8a. The same as Figure 7a for horizontal dimensions of 2.5°.

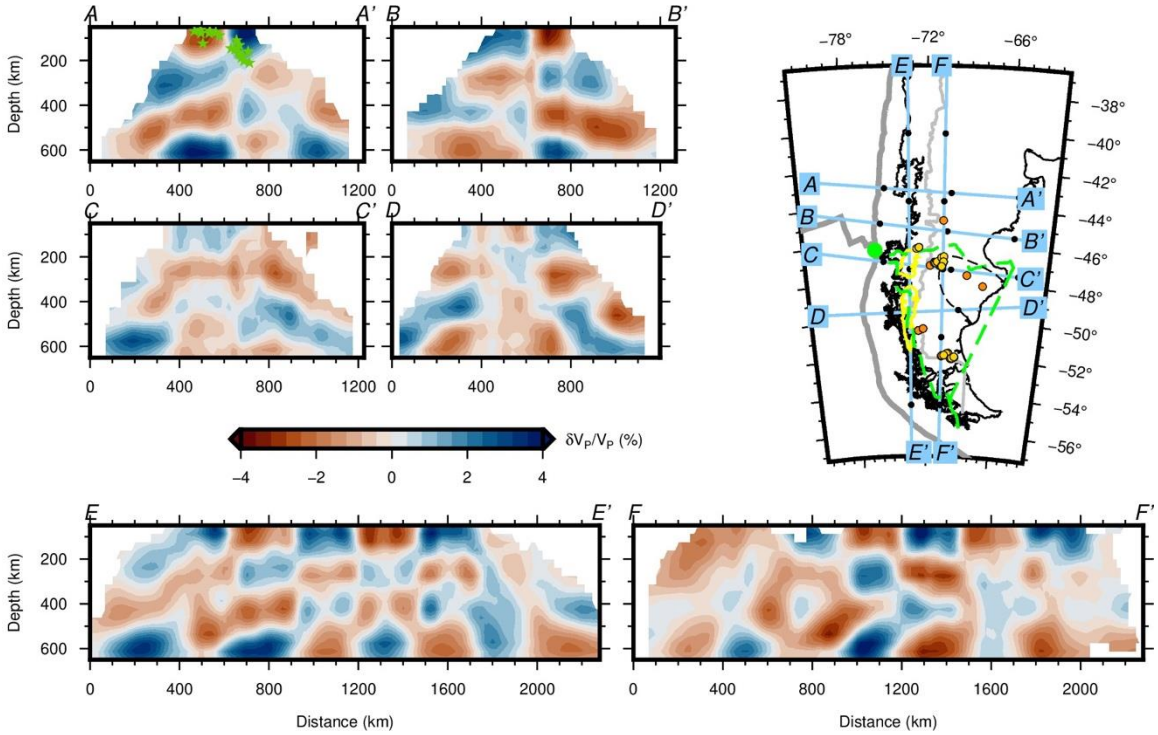

Figure S8b. Recovery for checkerboard test presented in Figure S8a. The recovery is slightly poorer than the recovery of the smaller cells shown in Figure S7b, showing that our data set combined with the multiscale parametrization approach is well suited for resolving small anomalies in appropriate regions despite limitations in resolving some larger scale features.

Structural tests

Fast velocity perturbation/Nazca slab

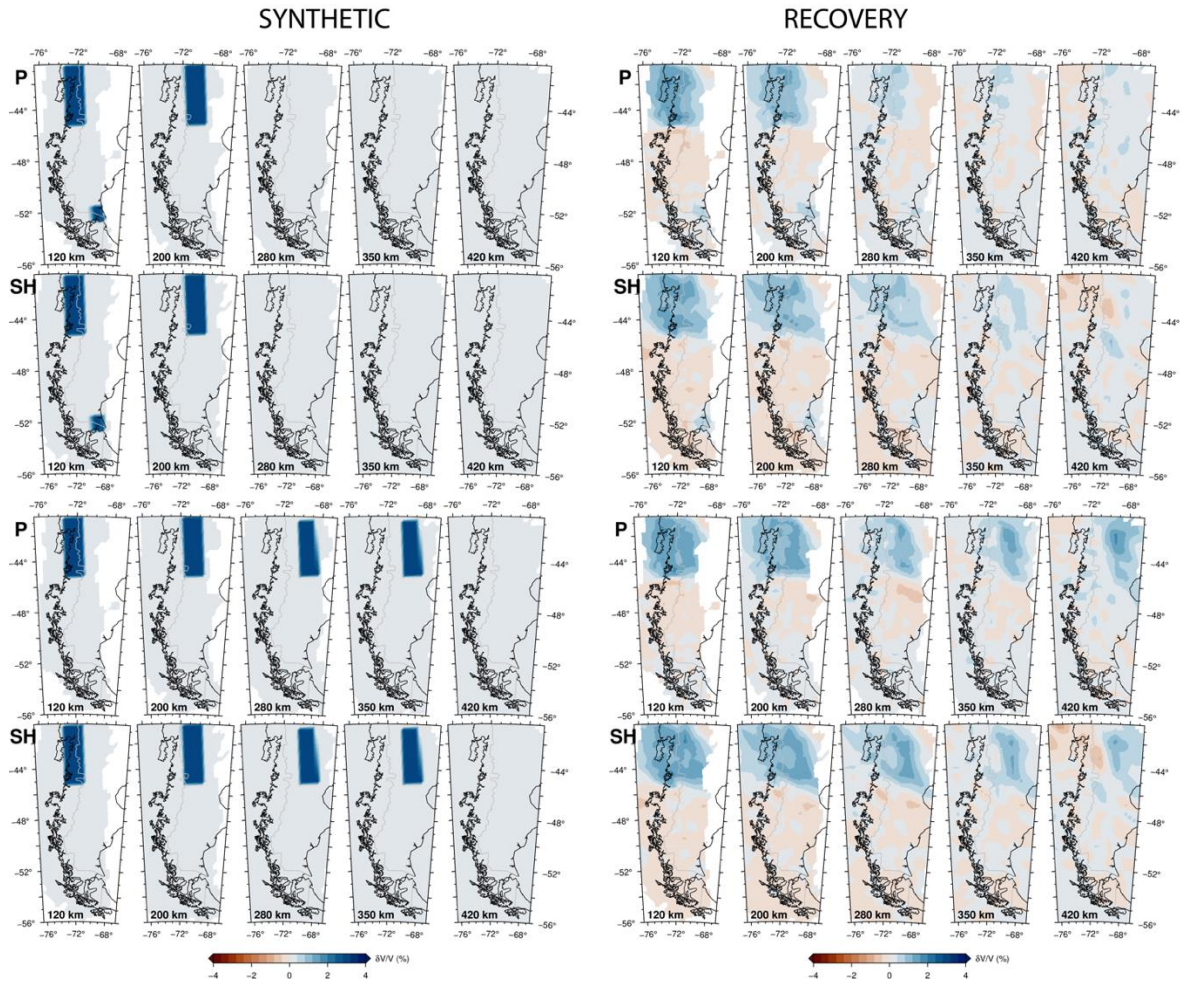

Figure S9. Synthetic and recovery results for P and SH waves associated with a fast velocity perturbation (+3%) between 40°S and 46°S simulating a 100km thick slab penetrating down to 200 km and 350km respectively.

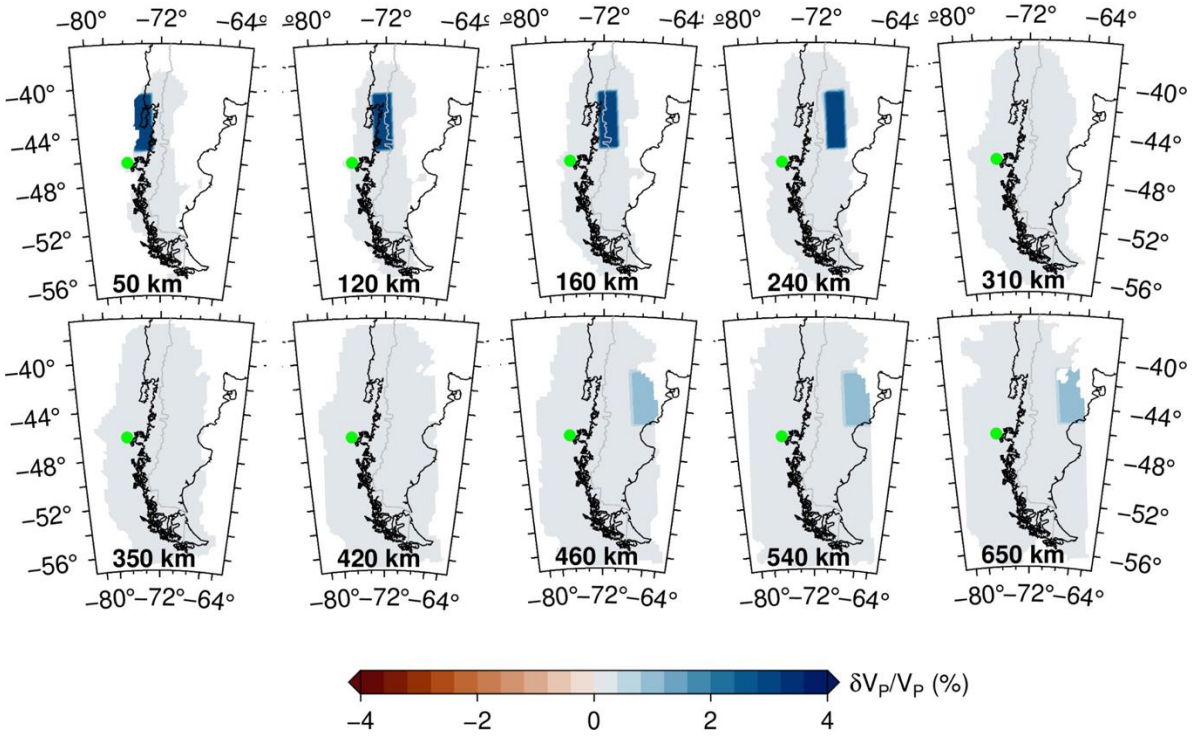

Figure S10a. Synthetic tests for P waves associated with a fast velocity perturbation (+4%) between 40°S and 46°S simulating a 100km thick slab penetrating down to 240 km and a fast velocity perturbation (+2%) between 460 km and 650 km depth

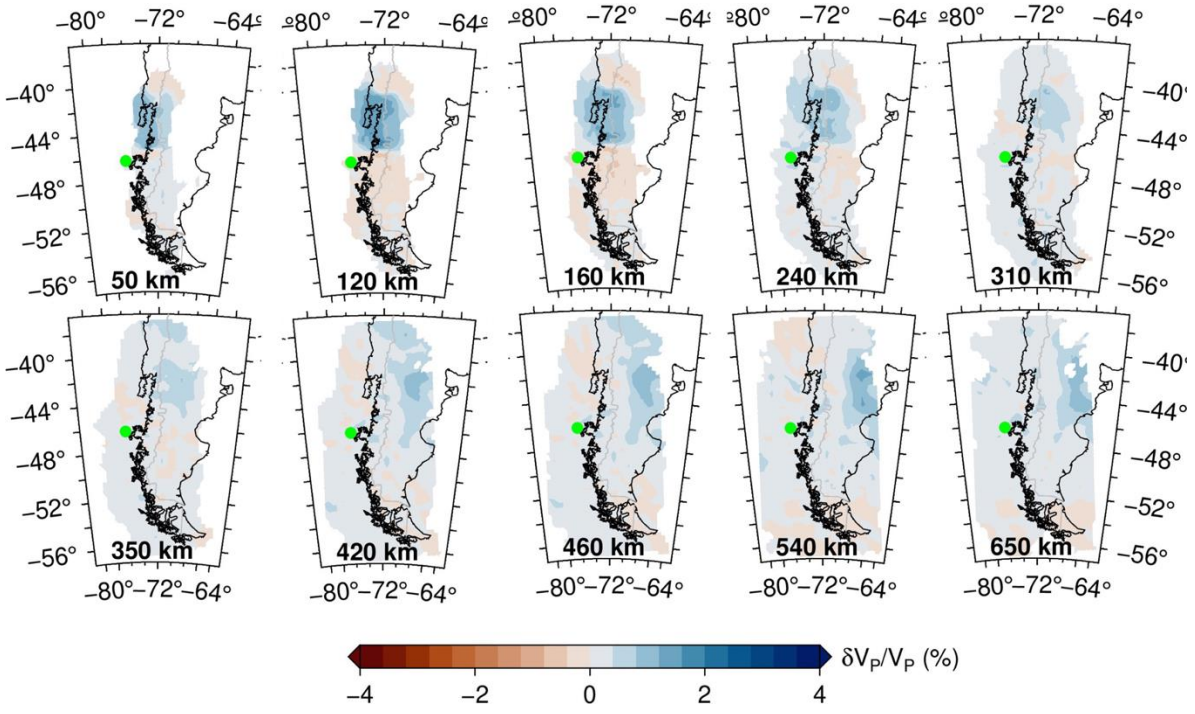

Figure S10b. Recovery results for P waves presented in Figure S10a.

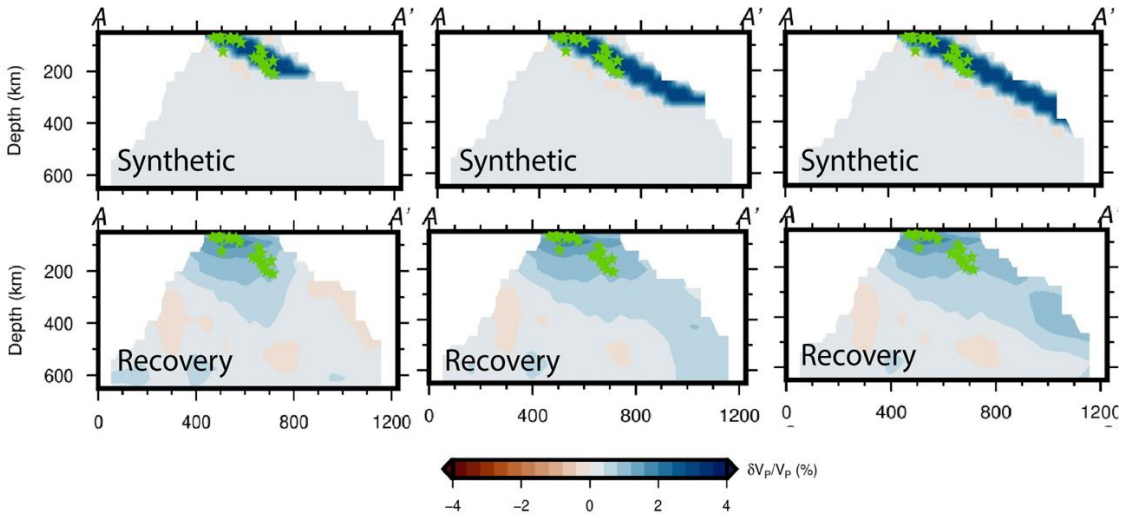

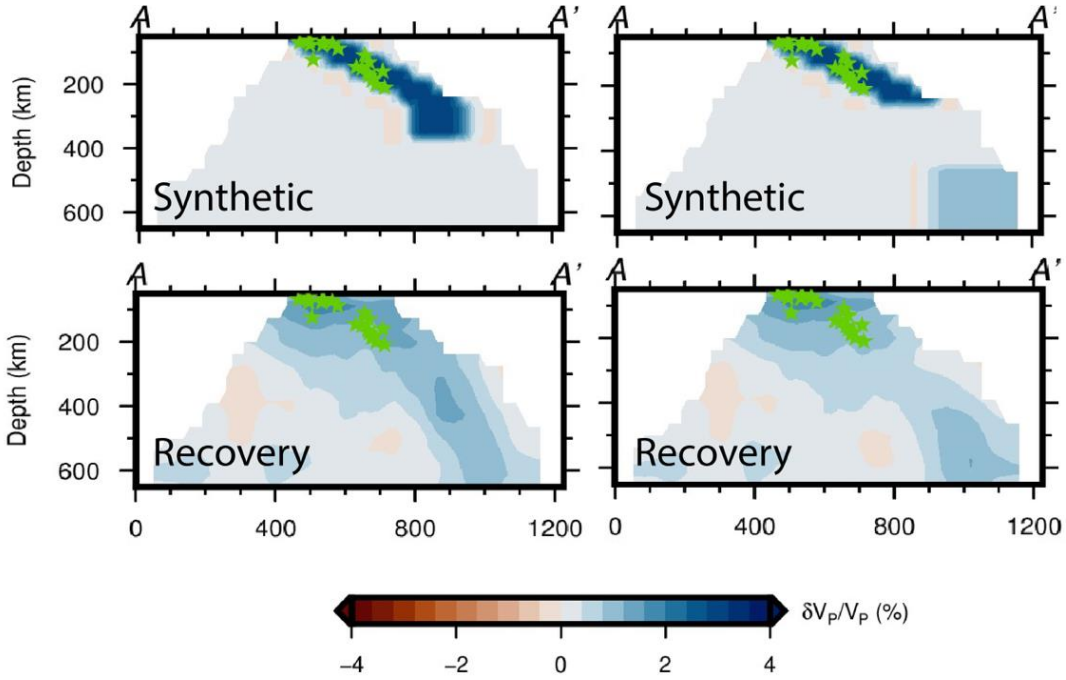

Figure S11. Synthetic and recovery results for P in cross section along the same profiles shown in Figure 3 in the manuscript associated with a 100km thick fast velocity perturbation (+4%) representing possible scenarios for the depth extension of the Nazca slab. Green stars represent earthquake from the US. Geological Survey catalogue (https://earthquake.usgs.gov/).

Slow velocity perturbation/Slab window

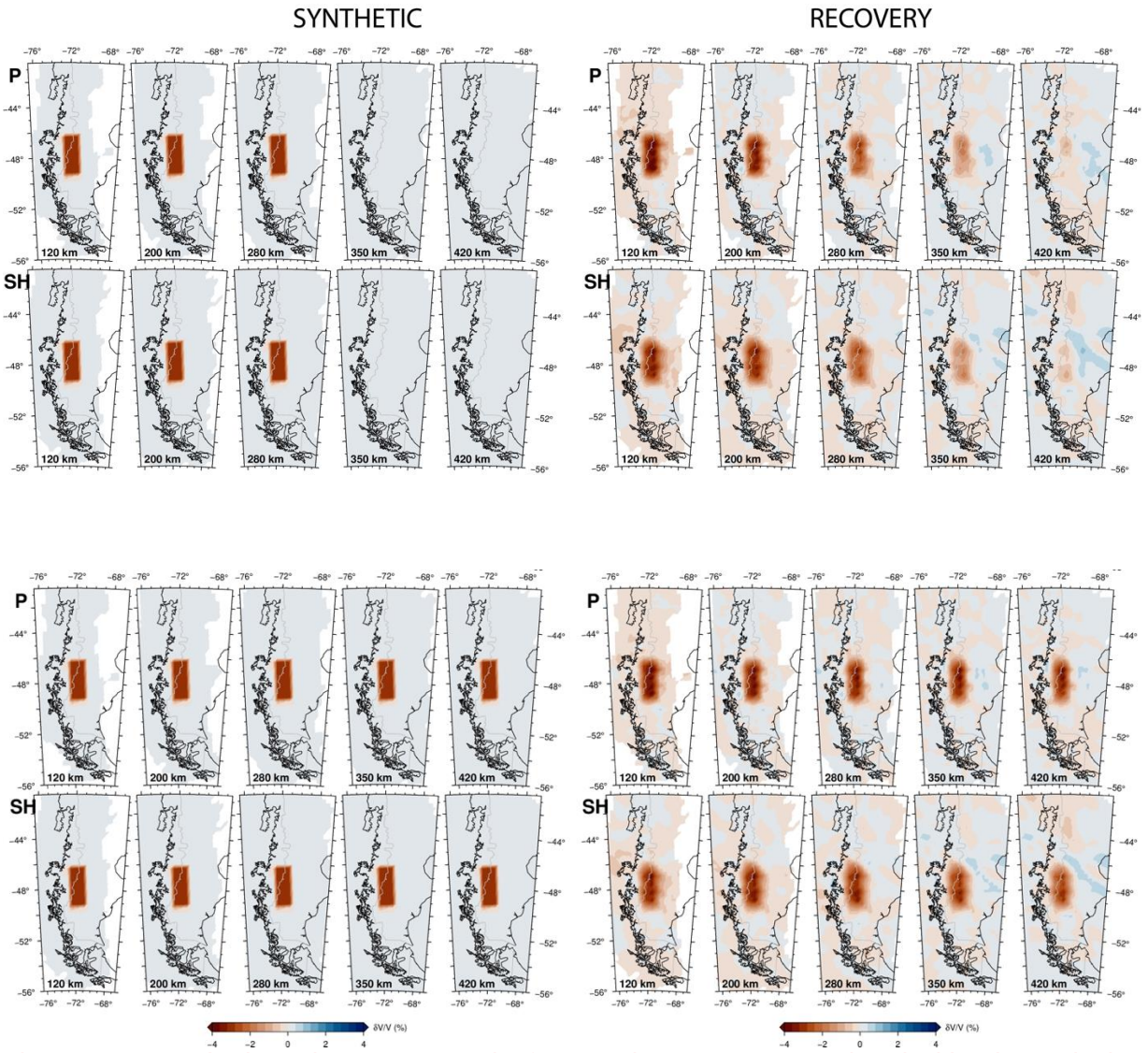

Figure S12. Synthetic and recovery results for P and SH waves associated with a low velocity perturbation (-3%) between 46°S and 49°S down to 280km and 420km depth respectively.

Two distinct low velocity perturbations/Slab window and one shallow fast velocity perturbation

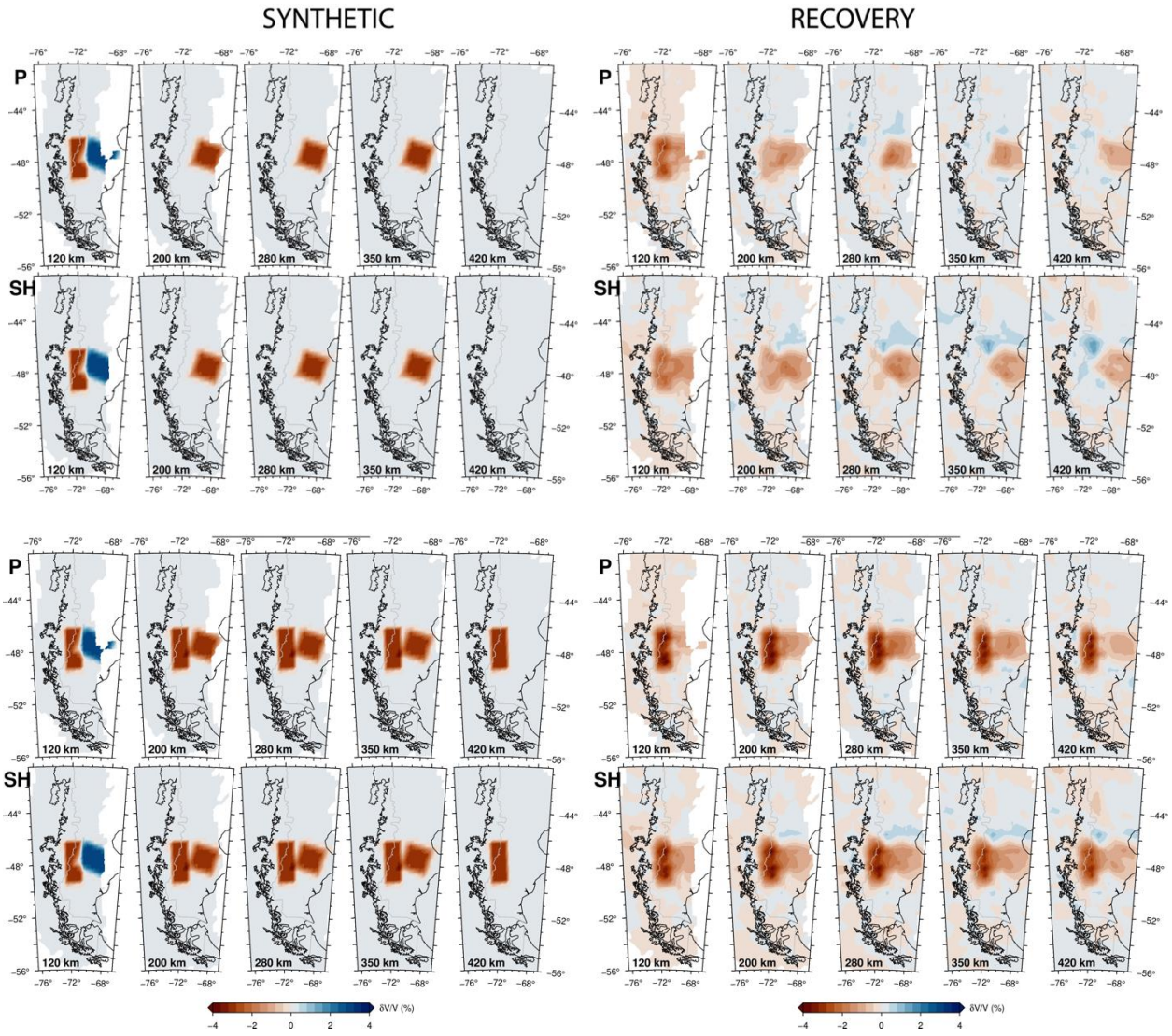

-

Figure S13. The same as Figure S12, except that the low velocity anomaly extends in the upper row only to 120 km depth, with addition to the east of the previous anomaly of a deep low velocity perturbation (-3%) and a shallow fast one (+3%).

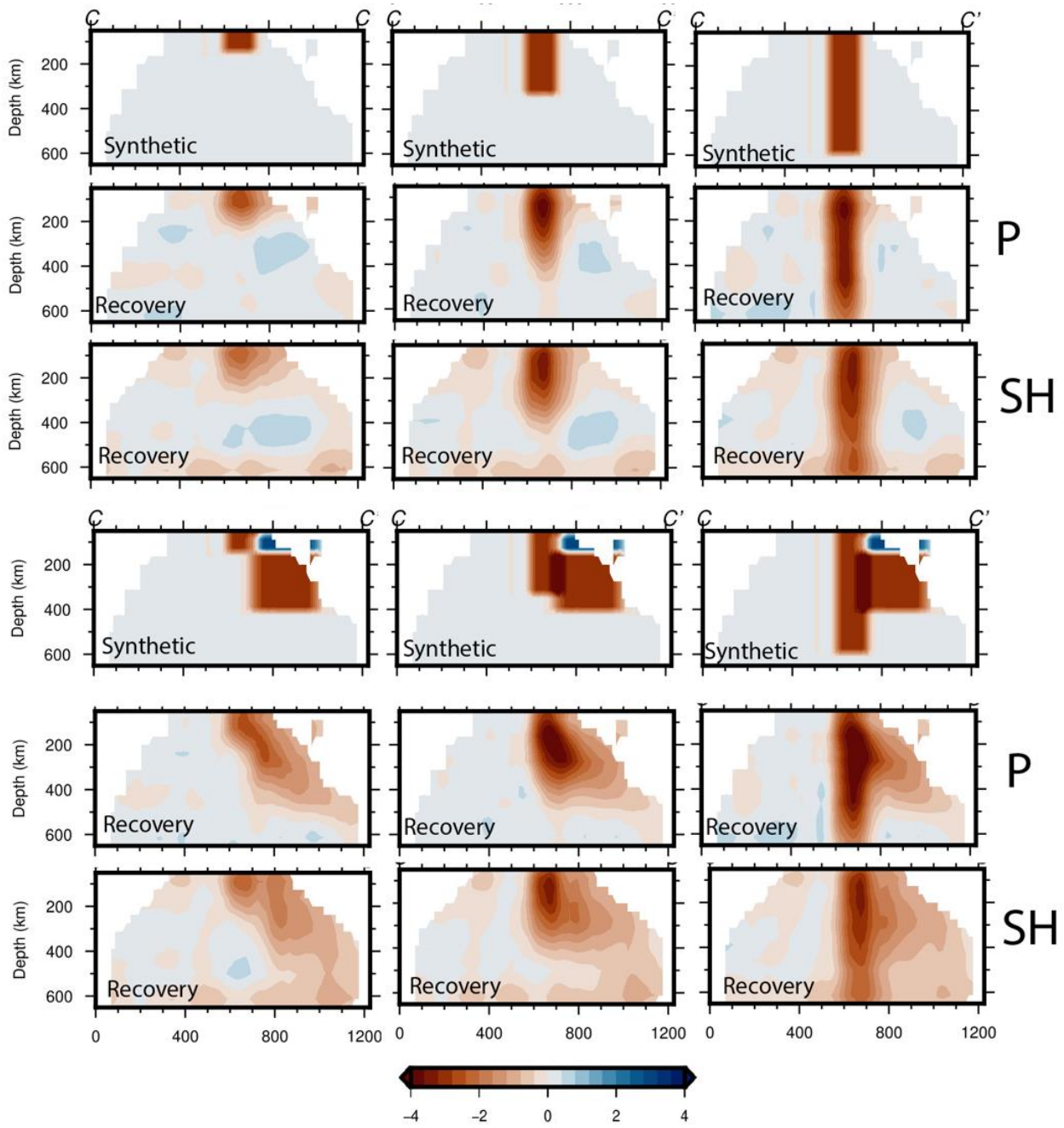

Figure S14. Vertical cross sections along the profile shown in Figure 3 in the manuscript for the resolution tests presented in Figure S12 and S13, with addition of two cases with an even deeper low velocity anomaly.

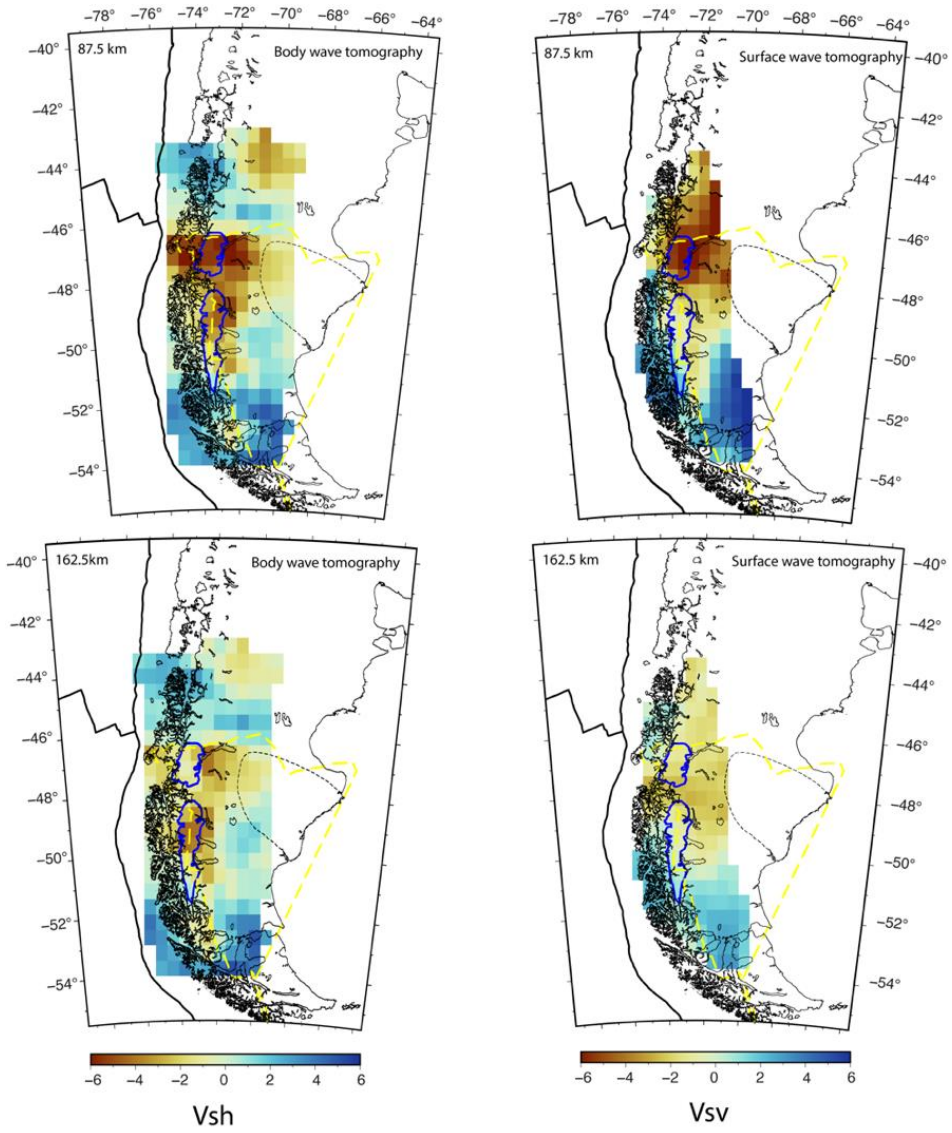

Figure S15. Comparison of shear wave structure at 87.5km (top) and 162.5km(bottom) derived from body wave tomography (this study) and surface wave tomography (Mark et al. 2022). The tectonic features on the map follow the same conventions as in Figure 2 in the manuscript.